

Zero-Shot Anomaly Detection with Dual-Branch Prompt Selection

Zihan Wang^{1,2}

zihan.wang5@mail.mcgill.ca

Samira Ebrahimi Kahou^{2,3,4}

samira.ebrahimikahou@ucalgary.ca

Narges Armanfard^{1,2}

narges.armanfard@mcgill.ca

¹ McGill University

Montreal, QC, Canada

² Mila – Quebec AI Institute

Montreal, QC, Canada

³ University of Calgary

Calgary, AB, Canada

⁴ CIFAR AI Chair

Canada

Accepted at BMVC 2025.

Abstract

Zero-shot anomaly detection (ZSAD) enables identifying and localizing defects in unseen categories by relying solely on generalizable features rather than requiring any labeled examples of anomalies. However, existing ZSAD methods, whether using fixed or learned prompts, struggle under domain shifts because their training data are derived from limited training domains and fail to generalize to new distributions. In this paper, we introduce PILOT, a framework designed to overcome these challenges through two key innovations: (1) a novel dual-branch prompt learning mechanism that dynamically integrates a pool of learnable prompts with structured semantic attributes, enabling the model to adaptively weight the most relevant anomaly cues for each input image; and (2) a label-free test-time adaptation strategy that updates the learnable prompt parameters using high-confidence pseudo-labels from unlabeled test data. Extensive experiments on 13 industrial and medical benchmarks demonstrate that PILOT achieves state-of-the-art performance in both anomaly detection and localization under domain shift.

1 Introduction

Anomaly detection and localization is critical in safety-critical applications, including industrial inspection and medical diagnostics, where timely identification of rare deviations from normal patterns can prevent costly failures and improve patient outcomes. Traditional anomaly detection methods include supervised approaches that require labeled anomalous examples and unsupervised techniques relying solely on normal data [8, 29, 35, 38, 39, 52]. Supervised methods require scarce and diverse anomaly labels, whereas unsupervised approaches avoid any need for anomalous samples by modeling only normal data, though they depend on comprehensive, representative normal data from the target domain [12]. Zero-shot

Anomaly Detection (ZSAD) has emerged as a powerful approach by leveraging pretrained vision–language models (VLMs) such as CLIP [50], which learns joint representations of images and text from large-scale image–text data, to identify anomalies in visual data without requiring any target-domain annotations of normal or anomalous samples.

Early successful ZSAD approaches utilized CLIP by designing explicit textual prompts that described both the object category and its condition, such as “normal bottle” or “anomalous transistor”. By crafting a large number of prompts that described relevant combinations of object category and condition, these methods enabled zero-shot classification and significantly outperformed vanilla CLIP baselines [15, 21, 51]. These approaches are known as fixed prompt methods because they rely on manually designed textual prompts. More recent methods have shifted towards a single learnable prompt, where the prompt itself is represented as a trainable embedding and optimized during training. This optimization is performed using auxiliary data, which refers to anomaly detection datasets that are separate from the target domain. For example, AnomalyCLIP [63] learns single object agnostic prompt embeddings to capture generic anomaly patterns, while AdaCLIP [10] further integrates visual knowledge into the prompt embeddings to enhance model adaptation.

Despite these advances, both fixed and single learnable prompt approaches remain vulnerable to domain shift, which refers to performance degradation when data distribution in the target domain differs significantly from training data. Although pretrained VLMs like CLIP have strong generalization ability, their performance can drop sharply when there are significant differences between the data seen during pretraining and the target environment [9, 23]. Even when learnable prompt embeddings are further trained on auxiliary anomaly detection datasets, that are different from the actual deployment domain, these models often struggle to represent the full diversity of possible anomalies or adapt to new categories encountered at test time. This limited generalization occurs for two main reasons: first, the auxiliary and target datasets may have significant distribution differences, as we empirically demonstrate in Appendix B.2; second, single prompt embeddings risk overfitting to the patterns and features specific to the auxiliary dataset, which further reduces their ability to handle unseen anomalies. As a result, prompts derived from narrowly defined auxiliary sources may fail to capture diverse visual features in the target data [46]. Therefore, to address these challenges, we introduce a framework that learns and dynamically weights multiple prompts, rather than relying on a fixed or single learnable prompt.

On the other hand, Test-Time Adaptation (TTA) techniques have demonstrated improved model robustness in various computer vision tasks by refining model parameters on unlabeled test data [41, 49, 53]. Although TTA is designed to address domain shift between training and test data, applying naive TTA strategies – without tailoring them to the specific task at hand – can inadvertently degrade performance. When used blindly, especially in tasks such as detection or localization, the adaptation process may optimize surrogate objectives that are misaligned with the true goals, often leading to suboptimal outcomes [42, 45, 55]. AnovL [49] was among the first to introduce TTA for anomaly localization refinement in ZSAD scenarios, but its focus is limited to localization and relies on fixed prompts. These limitations motivate us to explore how both anomaly detection and localization can be improved under domain shift by effectively utilizing unlabeled target data.¹

To address these challenges, we propose a novel framework, **P**rompt Learning with **I**ntegrated **L**abel-Free Test-Time Adaptation for **Z**erO-Sho**T** Anomaly Detection (**PILOT**), a framework designed to mitigate the limitations of current ZSAD methods under domain

¹We present the Related Works section in Section A of the Supplementary Material.

shift. Instead of relying on a single learnable prompt, PILOT constructs a pool of learnable prompts, allowing the prompts to adaptively learn from various anomalies present in the auxiliary dataset. This design enables the model to adaptively weight the most relevant prompts for each input image, allowing for more nuanced representations of diverse anomalies and supporting more effective TTA. During inference, our label-free test-time adaptation strategy updates all learnable prompts according to their alignment with each test image, using high-confidence pseudo-labels generated from unlabeled target data. This targeted adaptation facilitates rapid and reliable adjustment to new domains (i.e., the test domain) without requiring any labeled data. In addition, to mitigate overfitting to the auxiliary dataset and enhance adaptation stability, PILOT incorporates an attribute memory bank, which consists of a curated set of fixed prompts that describe normal and anomalous states, leveraging pre-trained semantic knowledge from the text encoder. This attribute memory bank serves as a semantic anchor, helping to stabilize localization performance during TTA. Together, these innovations enable PILOT to achieve robust anomaly detection and localization across a variety of challenging real-world scenarios. Our contributions are summarized as follows:

- We propose a dual-branch prompt learning framework that dynamically weight the most relevant prompts from both learnable prompt pool and attribute memory bank, enabling the model to leverage the most relevant anomaly cues for each input image.
- To our knowledge, this is the first label-free TTA strategy in ZSAD that leverages high-confidence pseudo-labels from unlabeled test samples to rapidly adapt prompt parameters at inference, yielding improvements in both anomaly detection and localization under domain shift.
- Extensive evaluation on industrial and medical benchmarks shows that our method outperforms existing approaches in both anomaly detection and localization metrics.

2 Proposed Method

ZSAD involves detecting and localizing anomalies in images from categories not encountered during the training phase. Formally, in the *training phase*, we employ an auxiliary dataset defined as $\mathcal{D}_{\text{aux}} = (I_i, y_i, G_i)_{i=1}^{|\mathcal{D}_{\text{aux}}|}$, where each image $I_i \in \mathbb{R}^{H \times W \times 3}$ is paired with an image-level label $y_i \in \{0, 1\}$ (0 denotes normal and 1 denotes anomalous) and a pixel-level anomaly mask

$G_i \in \{0, 1\}^{H \times W}$. In the *inference phase*, we consider an unlabeled target dataset $\mathcal{D}_{\text{tar}} = \{I_t\}_{t=1}^{|\mathcal{D}_{\text{tar}}|}$, where each $I_t \in \mathbb{R}^{H \times W \times 3}$. For every I_t , the model outputs an anomaly score $\hat{y}_t \in [0, 1]$, (with values closer to 1 indicating higher abnormality likelihood), along with a $\hat{G}_t \in [0, 1]^{H \times W}$ that spatially localizes potential anomalous regions at pixel level. Crucially, the category sets of \mathcal{D}_{aux} and \mathcal{D}_{tar} are strictly disjoint, ensuring that the target domain remains unseen during training and thus establishing a true zero-shot setting.

To address the limitations of existing approaches, we propose a dual-branch framework that combines a learnable prompt pool \mathcal{P} with an attribute memory bank \mathcal{U} . The training phase of our PILOT framework, depicted in Fig. 1, highlights these two key components. Further details on the inference phase are provided in Section 2.5, with in-depth descriptions of each component in the following sections and the complete pseudocode in Appendix E.

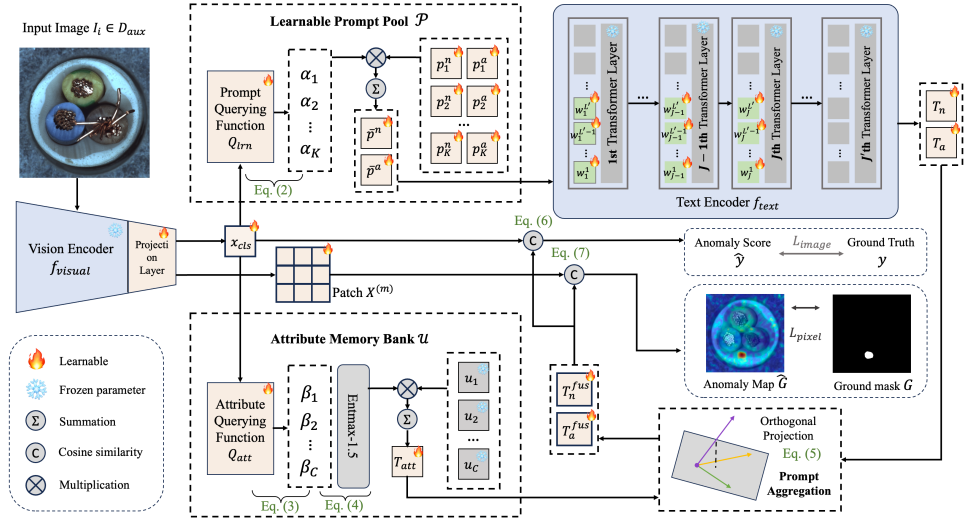


Figure 1: Overview of PILOT’s training phase. The left panel shows the main workflow. The right panel details the Learnable Prompt Pool \mathcal{P} and Attribute Memory Bank \mathcal{U} .

2.1 Learnable Prompt Pool

A successful recent approach for CLIP-based ZSAD employs a *single* learnable prompt, defined as a pair of sequences (p^n, p^a) representing normal and anomalous states, respectively, for binary anomaly classification [63]. Formally, this prompt can be represented as:

$$p^n = [v^1, \dots, v^L, \text{“[normal state] object”}], p^a = [v^1, \dots, v^L, \text{“[anomalous state] object”}] \quad (1)$$

where L is the number of learnable prefix vectors, and each $v^{(i)} \in \mathbb{R}^d$ is a d -dimensional vector trained jointly with the model. These vectors form a “soft prompt,” intuitively acting as special tokens whose values steer the model’s attention without modifying its core parameters, follows the prefix-tuning paradigm, which guides VLMs while keeping the main model weights frozen [66, 40]. The placeholders “[normal state]” and “[anomalous state]” filled with descriptors of the object’s condition, such as “flawless” and “damaged.”

Despite its simplicity and effectiveness, relying solely on a single learnable prompt for all input images limits generalization under domain shift, as discussed in the introduction, because a single pair of prompts often fails to adequately represent the diversity of anomaly patterns encountered in different scenarios. To address this limitation, we propose extending this single prompt to a learnable prompt *pool*, containing multiple learnable prompts, each associated with additional embeddings for adaptive weighting and alignment. Formally, the proposed prompt pool is defined as $\mathcal{P} = \{(p_k^n, p_k^a, s_k, r_k)\}_{k=1}^K$, where $K = |\mathcal{P}|$ is the cardinality of the prompt pool. Each (p_k^n, p_k^a) is constructed similarly to previous works, and the additional learnable embeddings s_k and r_k enable adaptive weighting of the prompts and alignment with the input image features. Here, s_k is a modulation vector for prompt k , applied element-wise to the image feature x_{cls} to adaptively emphasize information relevant to that prompt, while r_k provides a prompt-specific reference for measuring similarity. These embeddings facilitate an adaptive emphasis on prompts that best align with the diverse patterns present in the auxiliary dataset. To achieve this adaptive prompt weighting, we introduce a

prompt-querying function, which computes prompt relevance scores given an image feature $x_{\text{cls}} \in \mathbb{R}^d$ produced by the CLIP vision encoder, i.e. f_{visual} , from an image I_i in \mathcal{D}_{aux} :

$$Q_{\text{lm}}(x_{\text{cls}}, \mathcal{P}) = \left\{ \alpha_k := \text{sim}(x_{\text{cls}} \odot s_k, r_k) \right\}_{k=1}^K, \quad (2)$$

where “ \odot ” denotes element-wise multiplication, and $\text{sim}(\cdot, \cdot)$ represents cosine similarity. Intuitively, α_k quantifies how well the image content aligns with the k -th prompt pair; this is realized by weighting the image feature x_{cls} with the attention mask s_k and measuring its similarity to the associated reference embedding r_k . The higher the score α_k is, the more similar the input image is to the k -th prompt (p_k^n, p_k^a) . These scores are then used to form weighted combinations of the prompt token sequences as $\bar{p}^n = \sum_{k=1}^K \alpha_k p_k^n$, $\bar{p}^a = \sum_{k=1}^K \alpha_k p_k^a$. The resulting \bar{p}^n and \bar{p}^a are subsequently encoded using the CLIP pretrained text encoder to obtain the final text embeddings $T_n = f_{\text{text}}(\bar{p}^n)$ and $T_a = f_{\text{text}}(\bar{p}^a)$, which are employed for downstream anomaly scoring and localization. This process is visualized in Figure 1.

Although the text encoder f_{text} is frozen to preserve CLIP’s rich pretrained textual representations, we employ a prefix-tuning strategy to enable effective fine-tuning and adaptation of CLIP. Inspired by similar prefix-tuning methods [66], we introduce additional learnable parameters to f_{text} . More specifically, as is shown in Figure 1, layer-wise prefix vectors are defined as $\{w_j^{(\ell)} \in \mathbb{R}^d \mid j = 1, \dots, J, \ell = 1, \dots, L'\}$, where f_{text} consists of a total of J' transformer layers, and $J \leq J'$ denotes the number of initial layers to which learnable vectors are appended. L' represents the number of learnable vectors per layer. Specifically, these prefix vectors are prepended as additional tokens to the input sequence at the first J transformer layers, leaving the original transformer layers unchanged. At each layer j , these vectors $\{w_j^{(\ell)}\}_{\ell=1}^{L'}$ (illustrated as green blocks within the f_{text} module of Figure 1) are added before the standard, frozen token embeddings (represented as gray blocks in the f_{text} module of Figure 1) prior to the self-attention mechanism in each frozen transformer layer. This approach enables adaptation of the model’s internal representations without modifying the pretrained CLIP parameters, thereby preserving their robustness and generalization capabilities. Furthermore, as is illustrated in Figure 1, PILOT fine-tunes only the final d -dimensional projection layer within the vision encoder f_{visual} . By restricting updates exclusively to this projection layer, we substantially reduce memory overhead and computational complexity. This targeted fine-tuning strategy also mitigates the risk of overfitting to auxiliary datasets, maintaining the strong generalization properties inherent to CLIP [72].

2.2 Attribute Memory Bank

Although the learnable prompt pool \mathcal{P} aims to provide adaptive and diverse representations tailored to the auxiliary dataset, it may still be susceptible to overfitting when deployed on target domains. To mitigate this issue, we further introduce a fixed attribute memory bank comprising attribute embeddings extracted from the pretrained CLIP text encoder f_{text} (prior to applying our modifications). Recent works, such as WinCLIP [64], have demonstrated the robustness of fixed textual prompts by encoding multiple natural-language templates. Inspired by this, we construct our attribute memory bank from a set of descriptive natural-language templates (e.g., “A bright photo of a [State] object”), where [State] indicates descriptive attributes of the object’s condition (e.g., “normal”, “corroded”, or “contaminated”).

Each attribute template is passed through the frozen CLIP text encoder f_{text} , without any additional learnable tokens $w_j^{(\ell)}$, to produce a fixed attribute embedding, formally defined as

$\mathcal{U} = \{(u_c, g_c)\}_{c=1}^C$, where C is the number of attribute embeddings, and each $u_c \in \mathbb{R}^d$ represents the EOS-token embedding of the corresponding template. Unlike WinCLIP, which averages embeddings across multiple prompts, we associate each attribute embedding u_c with a learnable modulation vector g_c , similar to the learnable prompt pool. Similar to how s_k adapts the image features for each prompt, g_c dynamically modulates the contribution of each attribute according to the input image. Specifically, given an image feature x_{cls} , we introduce the attribute-querying function to compute attribute relevance scores as below:

$$\mathcal{Q}_{\text{att}}(x_{\text{cls}}, \mathcal{U}) = \{\beta_c := \text{sim}(x_{\text{cls}} \odot g_c, u_c)\}_{c=1}^C, \quad (3)$$

where “ \odot ” denotes element-wise multiplication, and $\text{sim}(\cdot, \cdot)$ is the cosine similarity. Here, u_c itself serves as the reference embedding for each attribute, as it is obtained directly from the pretrained f_{text} and already contains rich semantic information. Each score β_c quantifies the alignment between the image and the c -th attribute embedding. The resulting scores $\{\beta_c\}_{c=1}^C$ quantify the alignment between the input and each attribute. Following [60], we inject i.i.d. Gumbel noise into the attribute logits and apply the entmax 1.5 operator [60] to obtain a sparse yet differentiable weighting over the most prominent cues:

$$\{\phi_c\}_{c=1}^C = \text{entmax 1.5}(\beta_c + \text{noise}), \quad \sum_{c=1}^C \phi_c = 1, \quad \phi_c \geq 0. \quad (4)$$

We then compute the attribute text embedding as a weighted combination. $T_{\text{att}} = \sum_{c=1}^C \phi_c u_c$, $T_{\text{att}} \in \mathbb{R}^d$. The injected noise promotes exploration and prevents premature convergence to a single attribute, allowing the model to capture diverse and complementary semantic cues. By providing stable, pretrained semantic cues, the attribute memory bank acts as a semantic anchor during TTA discussed in Section 2.5. This mechanism helps to counteracts the potential overfitting and instability of learnable prompts, ensuring the model retains reliable semantic references even as it adapts to new domains.

2.3 Prompt Aggregation via Orthogonal Projection

Following [60], to robustly leverage both the stable semantics from the attribute embedding T_{att} and the adaptive semantics from the learnable prompts (T_n for normal and T_a for anomalous), we aggregate these representations using an orthogonal projection operation instead of simple averaging or concatenation. For each prompt embedding $T_{(\cdot)}$ (where $(\cdot) \in \{n, a\}$), we decompose it into components parallel and orthogonal to T_{att} :

$$T_{(\cdot)}^{\text{fus}} = T_{\text{att}} + (T_{(\cdot)} - \text{Proj}_{T_{\text{att}}}(T_{(\cdot)})), \quad \text{Proj}_{\eta}(\psi) = \frac{\eta^\top \psi}{\|\eta\|^2} \eta \quad (5)$$

This construction anchors the fused embedding in the robust attribute space, while enriching it with only those cues from the learnable prompt that are *complementary* to the attribute. Geometrically, $T_{(\cdot)}^{\text{fus}}$ preserves all the core semantics provided by T_{att} , and selectively incorporates novel information from $T_{(\cdot)}$ that lies in the orthogonal complement. Further analysis can be found in Appendix E.8. This parameter-free aggregation prevents redundancy and enhances robustness to distributional shift, especially during TTA, as shown in Table 11.

2.4 Training Objectives

To achieve both accurate anomaly detection and precise localization, we jointly optimize image-level classification and pixel-level segmentation objectives. Joint training allows the two tasks to reinforce each other, as global context aids localization while fine-grained cues improve classification. All training is performed on the auxiliary dataset \mathcal{D}_{aux} . Given the aggregated text embedding $T_{(\cdot)}^{fus}$ and the global visual feature x_{cls} , we compute the anomaly score and corresponding image-level loss:

$$\hat{y} = \sigma(\text{sim}(x_{cls}, T_{(\cdot)}^{fus})), \quad \mathcal{L}_{\text{image}} = \text{BCE}(\hat{y}, y) \quad (6)$$

where $\sigma(\cdot)$ denotes the sigmoid function, $\text{sim}(\cdot, \cdot)$ is cosine similarity, and BCE is the binary cross-entropy loss comparing the predicted score \hat{y} to the ground-truth image label $y \in \{0, 1\}$. For pixel-level localization, following [63], we extract patch features $\{X^{(m)} \in \mathbb{R}^{H \times W \times d}\}_{m \in \mathcal{M}}$ from a set \mathcal{M} of selected layers in f_{visual} . Each $X^{(m)}$ is formed by reshaping the patch token sequence into a spatial grid of size $H \times W$ with d -dimensional embeddings. For each $m \in \mathcal{M}$, we compute an anomaly map using the aggregated text embedding:

$$\hat{G}^{(m)} = \sigma(\text{sim}(X^{(m)}, T_{(\cdot)}^{fus})), \quad \mathcal{L}_{\text{pixel}} = \frac{1}{|\mathcal{M}|} \sum_{m \in \mathcal{M}} [\text{Focal}(\hat{G}^{(m)}, G) + \text{Dice}(\hat{G}^{(m)}, G)] \quad (7)$$

where $\hat{G}^{(m)} \in [0, 1]^{H \times W}$ is the predicted anomaly probability map for layer s , G is the ground-truth pixel-level mask, $\text{Focal}(\cdot, \cdot)$ denotes the focal loss [44], and $\text{Dice}(\cdot, \cdot)$ denotes the Dice loss [64]. This combination balances pixel-wise discrimination and overlap accuracy. The final training objective combines both terms $\mathcal{L}_{\text{PILOT}} = \mathcal{L}_{\text{image}} + \mathcal{L}_{\text{pixel}}$.

2.5 Test-Time Adaptation

A central challenge for robust ZSAD, as outlined in the Introduction, is achieving reliable adaptation to target domains that may differ significantly from the auxiliary dataset. While fine-tuning on \mathcal{D}_{aux} can calibrate model representations, substantial domain shifts often cause conventional approaches to overfit or fail to generalize, especially in the absence of labeled data from the target domain. To overcome these obstacles, we propose a TTA strategy that enables the model to adjust to new domains using only unlabeled target data, without compromising the integrity of previously learned representations.

The core idea of our TTA strategy is to identify a subset of highly reliable predictions (high-confidence pseudo-labels) from the target dataset and leverage these predictions to update model parameters. Specifically, for each image I_t in the unlabeled target dataset \mathcal{D}_{tar} , we compute the anomaly score as $\tilde{y}_t = \sigma(\text{sim}(x_{cls}^t, T_{(\cdot)}^{fus}))$, where x_{cls}^t is the CLIP visual feature for I_t and $T_{(\cdot)}^{fus}$ denotes the fused prompt embedding selected and aggregated for I_t using model parameters trained on \mathcal{D}_{aux} . We then identify the most reliable samples by selecting the top and bottom ρ -fractions of scores:

$$A = \text{Top}_{[\rho B]} \{\tilde{y}_t\}_{t=1}^B, \quad N = \text{Bot}_{[\rho B]} \{\tilde{y}_t\}_{t=1}^B, \quad (8)$$

where $B = |\mathcal{D}_{tar}|$ and $0 < \rho < 0.5$. Pseudo-labels are then defined by $\hat{y}_t = 1$ if $t \in A$, and $\hat{y}_t = 0$ if $t \in N$. Adaptation is performed by optimizing an image-level binary cross-entropy loss on the selected samples, i.e., $\mathcal{L}_{\text{image}} = \text{BCE}(\hat{y}_i, \tilde{y}_i)$ for $i \in A \cup N$.

Critically, during TTA, we update only the parameters associated with the learnable prompt pool, including the learnable prompts, their corresponding embeddings s_k and r_k . All other model parameters, such as those in the attribute memory bank and the core CLIP architecture, remain fixed. The updates for each learnable prompt are weighted by the attention scores defined previously (see Section 2.1), meaning prompts with higher attention scores for a given input contribute more significantly to parameter updates. We limit adaptation strictly to the image-level objective because, as shown in our experiments (Section 3.2), pseudo-labels derived at the image level exhibit considerably higher reliability compared to those at the pixel level. Pixel-level pseudo-labeling can be adversely affected by spatial ambiguity and noise exacerbated by domain shifts. By focusing adaptation solely on image-level labels, we reduce the risk of propagating noisy pseudo-labels, ensuring stable, unsupervised adaptation in the target domain. Our experimental results demonstrate that applying such a strategy improves both pixel-level and image-level detection on the target domain.

3 Experiments

Benchmarks. To demonstrate the effectiveness of our method, we conduct experiments on 13 widely used benchmarks spanning industrial inspection and medical imaging. Specifically, we evaluate on six industrial datasets: BTAD [48], VisA [64], MVTec AD [9], DAGM [69], SDD [66], and DTD-Synthetic [2] and seven medical datasets, subdivided into detection-only (HeadCT [67], BrainMRI [84], Br35H [27]) and localization (ISIC [47], CVC ColonDB [67], CVC ClinicDB [6], Kvasir [82]). The medical datasets for anomaly localization contain only anomalous samples and lack normal data; since our TTA strategy requires normal samples, results are reported without TTA (see Appendix H). To ensure strict zero-shot evaluation, auxiliary datasets exclude all target data. More specifically, for a fair comparison, we followed the related literature [11, 63], and used MVTec AD [9] as the auxiliary dataset when reporting the performance on all other datasets, while when reporting the performance on MVTec AD, we trained the model on VisA [64] as the auxiliary dataset.

Baseline. We compare PILOT with the most recent SOTA methods, including SAA[11], CoOp [61], WinCLIP [61], APRIL-GAN [14], AnomalyCLIP [63], and AdaCLIP [11].

Evaluation Metrics. Following standard practices in zero-shot anomaly detection literature such as [14, 63], we evaluated our method using the AUROC. Additionally, we report APs for anomaly detection and use AUPRO [9] to assess pixel-level anomaly localization performance. Results are provided at both dataset-level and domain-level averages.

3.1 Comparison with State-of-the-Art

As reported in Table 1, PILOT establishes state-of-the-art performance across all benchmarks for both image-level anomaly detection and pixel-level localization in the zero-shot setting. This can be benefited from PILOT comprehensive approach in addressing critical challenges prevalent in ZSAD, that explicitly tackles domain shift in test phase. Prior approaches [11, 61] rely solely on predefined prompts, which may not generalize well to unseen domains, whereas methods such as [11, 14, 61, 63] employ lightweight visual adapters or a single learnable prompt to capture anomaly cues, but often overfit to the auxiliary training set, limiting robustness under distribution shift. PILOT distinguishes itself by dynamically identifying the most relevant prompts for each input and refining only those learnable prompt parameters during inference using high-confidence pseudo-labels from the unlabeled target

Table 1: Model performance on public benchmarks. The top section reports image-level results (AUROC, AP), and the bottom section reports pixel-level results (AUROC, AUPRO). Best entries are marked with bold and second-best entries with underline.

Industrial Image-level Anomaly Detection (AUROC, AP)							
Dataset	SAA	CoCoOp	WinCLIP	APRIL-GAN	AnomalyCLIP	AdaCLIP	PILOT
MVTec AD	(64.2, 87.0)	(88.2, 94.5)	<u>(91.9, 96.4)</u>	(86.5, 93.2)	(91.6, 96.3)	(91.3, 95.8)	(92.1, 96.6)
VisA	(67.5, 76.2)	(63.2, 68.5)	(78.5, 81.4)	(78.2, 81.3)	<u>(81.8, 85.1)</u>	(81.6, 84.1)	(84.1, 85.7)
BTAD	(59.4, 89.2)	(67.0, 77.6)	(68.4, 71.1)	(73.8, 68.9)	(83.8, 88.4)	<u>(90.4, 90.7)</u>	(95.3, 96.8)
SDD	(68.9, 37.9)	(75.1, 65.3)	(84.5, 77.6)	(80.0, 71.7)	<u>(85.5, 81.7)</u>	(81.4, 72.8)	(87.9, 85.7)
DAGM	(87.3, 88.6)	(87.7, 74.8)	(91.9, 79.7)	(94.6, 84.0)	(96.1, 90.2)	<u>(97.3, 93.1)</u>	(98.5, 92.8)
DTD-Synthetic	(94.6, 93.7)	(92.4, 94.8)	(93.4, 92.8)	(86.7, 95.2)	(93.7, 97.3)	<u>(97.5, 98.2)</u>	(97.7, 98.4)
Mean	(73.7, 78.8)	(78.9, 79.3)	(84.8, 83.2)	(83.3, 82.4)	(88.8, <u>89.8</u>)	<u>(89.9, 89.1)</u>	(92.6, 92.7)
Medical Image-level Anomaly Detection (AUROC, AP)							
HeadCT	(46.8, 68.0)	(78.4, 78.8)	(81.8, 80.2)	(89.1, 89.4)	<u>(91.0, 92.3)</u>	(86.5, 81.3)	(94.5, 96.0)
BrainMRI	(34.4, 76.7)	(61.3, 44.9)	(86.6, 91.5)	(89.3, 90.9)	<u>(93.2, 94.7)</u>	(93.2, 89.7)	(97.3, 97.9)
Br35H	(33.2, 67.3)	(86.0, 87.5)	(80.5, 82.2)	(93.1, 92.9)	<u>(95.3, 96.0)</u>	(92.1, 90.9)	(96.7, 97.7)
Mean	(38.1, 70.7)	(75.2, 70.4)	(83.0, 84.6)	(90.5, 91.1)	<u>(93.2, 94.3)</u>	(90.6, 87.3)	(96.2, 97.2)
Industrial Pixel-level Anomaly Localization (AUROC, AUPRO)							
MVTec AD	(75.5, 38.1)	(44.4, 11.1)	(85.1, 64.6)	(87.6, 44.0)	(90.7, 78.7)	(89.4, 37.8)	<u>(90.3, 80.2)</u>
VisA	(76.5, 31.6)	(42.1, 12.2)	(79.6, 56.8)	(94.2, 86.8)	(95.3, 85.1)	<u>(95.5, 77.8)</u>	(96.0, 87.2)
BTAD	(65.8, 14.8)	(28.1, 6.5)	(72.7, 27.3)	(60.8, 25.0)	(94.4, 73.6)	(94.8, 32.5)	(96.3, 74.9)
SDD	(78.8, 6.6)	(24.4, 8.3)	(68.8, 24.2)	(79.8, 65.1)	<u>(90.7, 66.6)</u>	(71.7, 17.6)	(92.4, 73.4)
DAGM	(62.7, 32.6)	(17.5, 2.1)	(87.6, 65.7)	(82.4, 66.2)	<u>(95.6, 91.0)</u>	(91.1, 62.3)	(96.0, 91.4)
DTD-Synthetic	(76.7, 60.6)	(14.8, 3.0)	(83.9, 57.8)	(95.3, 86.9)	(97.8, 91.1)	(98.2, 86.2)	<u>(98.0, 90.2)</u>
Mean	(72.7, 30.7)	(28.6, 7.2)	(79.6, 49.4)	(83.4, 62.3)	<u>(94.1, 81.0)</u>	(90.1, 52.4)	(94.8, 82.9)

data. Note that while existing baselines can utilize the proposed image-level TTA strategies, these often degrade pixel-level localization performance and do not yield consistent improvements across both detection and localization tasks. On the contrary, PILOT uniquely achieves gains in both image-level and pixel-level metrics under TTA, a phenomenon analyzed in detail in Section 3.2. We also compare against state-of-the-art full-shot methods in Appendix F.1, which show that PILOT achieves image-level accuracy on par.

3.2 Effect of Test-Time Adaptation

Table 2 presents a comparison of all methods evaluated under a unified TTA protocol, where each method adapts learnable parameters across the test set using high-confidence pseudo-labels following PILOT’s label-free strategy. This fair setup reveals a key limitation of image-level TTA strategies in existing ZSAD models: while they can yield modest improvements in detection, they often destabilize pixel-level localization due to indiscriminate parameter updates guided by global objectives. This is particularly evident in methods like AnomalyCLIP, which use a single learnable prompt across all test images. In these cases, high-confidence pseudo-labels are often insufficient to represent the diversity of anomaly patterns in the target domain, resulting in imbalanced adaptation (see Appendix F.2) and degraded fine-grained localization. Thus, image-level TTA alone struggles to maintain the alignment between visual and semantic cues necessary for precise localization, especially in complex scenarios. Another significant limitation is conventional TTA methods’ susceptibility to noisy pseudo-labels, which propagate errors and degrade both detection and localization performance. PILOT’s adaptive prompt weighting addresses this by localizing

Table 2: Comparison of PILOT vs. state-of-the-art on industrial benchmarks. **Img** and **Pix** denote image-level and pixel-level metrics, respectively. “w/o TTA” and “w/ TTA” indicate performance without and with TTA, respectively. Arrows indicate change in performance: \uparrow (increase > 0.5), \downarrow (decrease < -0.5), and \circ (no significant change, ± 0.5).

Dataset		APRIL-GAN		AnomalyCLIP		AdaCLIP		PILOT	
		w/o TTA	w/ TTA	w/o TTA	w/ TTA	w/o TTA	w/ TTA	w/o TTA	w/ TTA
MVTec AD	Img	(86.5, 93.2)	(82.9 \downarrow , 89.8 \downarrow)	(91.6, 96.3)	(89.2 \downarrow , 95.0 \downarrow)	(91.3, 95.8)	(90.1 \downarrow , 95.8 \circ)	(90.2, 95.7)	(92.1 \uparrow , 96.6 \uparrow)
	Pix	(87.6, 44.0)	(86.0 \downarrow , 42.0 \downarrow)	(90.7, 78.7)	(88.1 \downarrow , 73.5 \downarrow)	(89.4, 37.8)	(87.0 \downarrow , 29.5 \downarrow)	(89.4, 79.2)	(90.3 \uparrow , 80.2 \uparrow)
VisA	Img	(78.2, 81.3)	(84.5 \uparrow , 88.0 \uparrow)	(81.8, 85.1)	(84.3 \uparrow , 85.8 \uparrow)	(81.6, 84.1)	(83.0 \uparrow , 85.0 \uparrow)	(82.0, 84.1)	(84.1 \uparrow , 85.7 \uparrow)
	Pix	(94.2, 86.8)	(92.0 \downarrow , 84.0 \downarrow)	(95.3, 85.1)	(85.5 \downarrow , 82.6 \downarrow)	(95.5, 77.8)	(93.8 \downarrow , 72.6 \downarrow)	(94.8, 85.6)	(96.0 \uparrow , 87.2 \uparrow)
BTAD	Img	(73.8, 68.9)	(76.9 \uparrow , 73.2 \uparrow)	(83.8, 88.4)	(85.7 \uparrow , 93.0 \uparrow)	(90.4, 90.7)	(91.6 \uparrow , 92.5 \uparrow)	(90.0, 91.6)	(95.3 \uparrow , 96.8 \uparrow)
	Pix	(60.8, 25.0)	(58.0 \downarrow , 23.0 \downarrow)	(94.4, 73.6)	(94.1 \circ , 72.0 \downarrow)	(94.8, 32.5)	(93.0 \downarrow , 25.5 \downarrow)	(94.9, 73.0)	(96.3 \uparrow , 74.9 \uparrow)
SDD	Img	(80.0, 71.7)	(79.9 \circ , 71.6 \circ)	(85.5, 81.7)	(85.7 \circ , 81.8 \circ)	(81.4, 72.8)	(83.0 \uparrow , 74.0 \uparrow)	(87.3, 85.2)	(87.9 \uparrow , 85.7 \uparrow)
	Pix	(79.8, 65.1)	(77.5 \downarrow , 63.0 \downarrow)	(90.7, 66.6)	(89.9 \downarrow , 63.8 \downarrow)	(71.7, 17.6)	(66.7 \downarrow , 12.5 \downarrow)	(88.7, 69.6)	(92.4 \uparrow , 73.4 \uparrow)
DAGM	Img	(94.6, 84.0)	(95.0 \circ , 84.5 \circ)	(96.1, 90.2)	(97.3 \uparrow , 92.0 \uparrow)	(97.3, 93.1)	(96.8 \circ , 92.2 \circ)	(97.1, 91.8)	(98.5 \uparrow , 92.8 \uparrow)
	Pix	(82.4, 66.2)	(80.5 \downarrow , 64.0 \downarrow)	(95.6, 91.0)	(93.1 \downarrow , 90.2 \downarrow)	(91.1, 62.3)	(90.2 \downarrow , 58.8 \downarrow)	(95.8, 91.8)	(96.0 \circ , 91.4 \circ)
DTD-Synthetic	Img	(86.7, 95.2)	(85.0 \downarrow , 93.5 \downarrow)	(93.7, 97.3)	(93.2 \circ , 96.9 \circ)	(97.5, 98.2)	(97.5 \circ , 98.4 \circ)	(95.3, 98.0)	(97.7 \uparrow , 98.4 \uparrow)
	Pix	(95.3, 86.9)	(93.5 \downarrow , 84.5 \downarrow)	(97.8, 91.1)	(93.3 \downarrow , 83.4 \downarrow)	(98.2, 86.5)	(94.9 \downarrow , 73.3 \downarrow)	(97.3, 89.9)	(98.0 \uparrow , 90.2 \circ)

the impact of label noise—updates concentrate on prompts closely aligned with each input, thus minimizing negative effects on the overall prompt pool.

3.3 Module Ablation

Table 3: Module ablation for PILOT on industrial datasets. **SLP**: Single Learnable Prompt; **+Attr**: SLP + Attribute Memory Bank; **Full**: SLP + Attr + Query & Prompt Pool (Full model). Metrics: Image = (AUROC, AP), Pixel = (AUROC, AUPRO).

	Image-Level		Pixel-Level	
	w/o TTA	w/ TTA	w/o TTA	w/ TTA
SLP	(90.8, 91.6)	(91.4 \uparrow , 91.9 \circ)	(94.2, 82.1)	(90.7 \downarrow , 79.8 \downarrow)
+Attr	(90.5, 91.3)	(91.2 \uparrow , 91.7 \circ)	(93.9, 81.5)	(94.0 \circ , 81.5 \circ)
Full	(90.3, 91.1)	(92.6 \uparrow , 92.7 \uparrow)	(93.5, 81.5)	(94.8 \uparrow , 82.9 \uparrow)

Table 3 evaluates individual components of PILOT across industrial datasets, highlighting how our design stabilizes pixel-level predictions during TTA. Using a single prompt, similar to existing ZSAD methods, improves detection but severely degrades localization accuracy due to the lack of spatial supervision, causing visual-textual misalignment. Introducing the fixed attribute memory bank addresses this by providing stable semantic anchors, constraining model adaptation and preserving localization quality through parameter-free orthogonal projection. The complete PILOT framework integrates prompts from the learnable pool and attribute memory bank through a dual-branch fusion mechanism, dynamically weighted by adaptive query functions. During TTA, parameter updates are guided by alignment scores, ensuring prompts aligned with high-confidence samples undergo more substantial refinement. This adaptive update strategy mitigates negative transfer risks from unseen data, enhancing both image-level detection and pixel-level localization.

4 Conclusion

We have introduced PILOT, a ZSAD framework designed to address domain shifts by adaptively integrating anomaly cues through a dual-branch prompt aggregation mechanism, which

combines a learnable prompt pool with semantic attribute embeddings. Our image-level TTA strategy further refines the prompt parameters using high-confidence pseudo-labels from unlabeled target data. Extensive experiments on 13 public benchmarks demonstrate that PI-LOT consistently achieves state-of-the-art performance in both anomaly detection and localization. Future work may explore advanced TTA strategies to jointly improve pixel-level localization and image-level detection, further enhancing ZSAD robustness.

Acknowledgements

The authors wish to acknowledge the financial support of McGill University, the Natural Sciences and Engineering Research Council of Canada (NSERC), and the Fonds de Recherche du Québec – Nature et technologies (FRQNT). We also acknowledge the computing resources provided by Calcul Québec and the Digital Research Alliance of Canada.

References

- [1] Toshimichi Aota, Lloyd Teh Tzer Tong, and Takayuki Okatani. Zero-shot versus many-shot: Unsupervised texture anomaly detection. In *Proceedings of the IEEE/CVF Winter Conference on Applications of Computer Vision*, pages 5564–5572, 2023.
- [2] Toshimichi Aota, Lloyd Teh Tzer Tong, and Takayuki Okatani. Zero-shot versus many-shot: Unsupervised texture anomaly detection. In *Proceedings of the IEEE/CVF Winter Conference on Applications of Computer Vision*, pages 5564–5572, 2023.
- [3] John Arevalo, Thamar Solorio, Manuel Montes-y Gómez, and Fabio A González. Gated multimodal units for information fusion. *arXiv preprint arXiv:1702.01992*, 2017.
- [4] Paul Bergmann, Michael Fauser, David Sattlegger, and Carsten Steger. Mvtec ad—a comprehensive real-world dataset for unsupervised anomaly detection. In *Proceedings of the IEEE/CVF conference on computer vision and pattern recognition*, pages 9592–9600, 2019.
- [5] Paul Bergmann, Michael Fauser, David Sattlegger, and Carsten Steger. Uninformed students: Student-teacher anomaly detection with discriminative latent embeddings. In *Proceedings of the IEEE/CVF conference on computer vision and pattern recognition*, pages 4183–4192, 2020.
- [6] Jorge Bernal, F Javier Sánchez, Gloria Fernández-Esparrach, Debora Gil, Cristina Rodríguez, and Fernando Vilariño. Wm-dova maps for accurate polyp highlighting in colonoscopy: Validation vs. saliency maps from physicians. *Computerized medical imaging and graphics*, 43:99–111, 2015.
- [7] Shirsha Bose, Ankit Jha, Enrico Fini, Mainak Singha, Elisa Ricci, and Biplab Banerjee. Styliip: Multi-scale style-conditioned prompt learning for clip-based domain generalization. In *Proceedings of the IEEE/CVF Winter Conference on Applications of Computer Vision*, pages 5542–5552, 2024.

- [8] Jakob Božić, Domen Tabernik, and Danijel Skočaj. Mixed supervision for surface-defect detection: From weakly to fully supervised learning. *Computers in Industry*, 129:103459, 2021.
- [9] Yunkang Cao, Xiaohao Xu, Zhaoge Liu, and Weiming Shen. Collaborative discrepancy optimization for reliable image anomaly localization. *IEEE Transactions on Industrial Informatics*, 19(11):10674–10683, 2023.
- [10] Yunkang Cao, Xiaohao Xu, Chen Sun, Yuqi Cheng, Zongwei Du, Liang Gao, and Weiming Shen. Segment any anomaly without training via hybrid prompt regularization. *arXiv preprint arXiv:2305.10724*, 2023.
- [11] Yunkang Cao, Jiangning Zhang, Luca Frittoli, Yuqi Cheng, Weiming Shen, and Giacomo Boracchi. Adacclip: Adapting clip with hybrid learnable prompts for zero-shot anomaly detection. In *European Conference on Computer Vision*, pages 55–72. Springer, 2024.
- [12] Varun Chandola, Arindam Banerjee, and Vipin Kumar. Anomaly detection: A survey. *ACM computing surveys (CSUR)*, 41(3):1–58, 2009.
- [13] Chun-Fu Richard Chen, Quanfu Fan, and Rameswar Panda. Crossvit: Cross-attention multi-scale vision transformer for image classification. In *Proceedings of the IEEE/CVF international conference on computer vision*, pages 357–366, 2021.
- [14] Xuhai Chen, Yue Han, and Jiangning Zhang. April-gan: A zero-/few-shot anomaly classification and segmentation method for cvpr 2023 vand workshop challenge tracks 1&2: 1st place on zero-shot ad and 4th place on few-shot ad. *arXiv preprint arXiv:2305.17382*, 2023.
- [15] Xuhai Chen, Jiangning Zhang, Guanzhong Tian, Haoyang He, Wuhao Zhang, Yabiao Wang, Chengjie Wang, and Yong Liu. Clip-ad: A language-guided staged dual-path model for zero-shot anomaly detection. In *International Joint Conference on Artificial Intelligence*, pages 17–33. Springer, 2024.
- [16] Noel CF Codella, David Gutman, M Emre Celebi, Brian Helba, Michael A Marchetti, Stephen W Dusza, Aadi Kalloo, Konstantinos Liopyris, Nabin Mishra, Harald Kittler, et al. Skin lesion analysis toward melanoma detection: A challenge at the 2017 international symposium on biomedical imaging (isbi), hosted by the international skin imaging collaboration (isic). In *2018 IEEE 15th international symposium on biomedical imaging (ISBI 2018)*, pages 168–172. IEEE, 2018.
- [17] Marc Botet Colomer, Pier Luigi Dovesi, Theodoros Panagiotakopoulos, Joao Frederico Carvalho, Linus Härenstam-Nielsen, Hossein Azizpour, Hedvig Kjellström, Daniel Cremers, and Matteo Poggi. To adapt or not to adapt? real-time adaptation for semantic segmentation. In *Proceedings of the IEEE/CVF International Conference on Computer Vision*, pages 16548–16559, 2023.
- [18] Hanqiu Deng and Xingyu Li. Anomaly detection via reverse distillation from one-class embedding. In *Proceedings of the IEEE/CVF conference on computer vision and pattern recognition*, pages 9737–9746, 2022.

- [19] Hanqiu Deng, Zhaoxiang Zhang, Jinan Bao, and Xingyu Li. Anovl: Adapting vision-language models for unified zero-shot anomaly localization. *arXiv preprint arXiv:2308.15939*, 2(5), 2023.
- [20] Matthijs Douze, Alexandr Guzhva, Chengqi Deng, Jeff Johnson, Gergely Szilvasy, Pierre-Emmanuel Mazaré, Maria Lomeli, Lucas Hosseini, and Hervé Jégou. The faiss library. 2024.
- [21] Sepideh Esmaeilpour, Bing Liu, Eric Robertson, and Lei Shu. Zero-shot out-of-distribution detection based on the pre-trained model clip. In *Proceedings of the AAAI conference on artificial intelligence*, volume 36, pages 6568–6576, 2022.
- [22] Mohammad Fahes, Tuan-Hung Vu, Andrei Bursuc, Patrick Pérez, and Raoul de Charette. Fine-tuning clip’s last visual projector: A few-shot cornucopia. *arXiv preprint arXiv:2410.05270*, 2024.
- [23] Ruoyu Feng, Tao Yu, Xin Jin, Xiaoyuan Yu, Lei Xiao, and Zhibo Chen. Rethinking domain adaptation and generalization in the era of clip. In *2024 IEEE International Conference on Image Processing (ICIP)*, pages 2585–2591. IEEE, 2024.
- [24] Sachin Goyal, Mingjie Sun, Aditi Raghunathan, and J Zico Kolter. Test time adaptation via conjugate pseudo-labels. *Advances in Neural Information Processing Systems*, 35: 6204–6218, 2022.
- [25] Arthur Gretton, Karsten M Borgwardt, Malte J Rasch, Bernhard Schölkopf, and Alexander Smola. A kernel two-sample test. *The Journal of Machine Learning Research*, 13(1):723–773, 2012.
- [26] Zhaopeng Gu, Bingke Zhu, Guibo Zhu, Yingying Chen, Ming Tang, and Jinqiao Wang. Anomalygpt: Detecting industrial anomalies using large vision-language models. In *Proceedings of the AAAI conference on artificial intelligence*, volume 38, pages 1932–1940, 2024.
- [27] A. Hamada. Br35h: Brain tumor detection 2020. <https://www.kaggle.com/datasets/ahmedhamada0/brain-tumor-detection>, 2020. Accessed: [insert access date].
- [28] Martin Heusel, Hubert Ramsauer, Thomas Unterthiner, Bernhard Nessler, and Sepp Hochreiter. Gans trained by a two time-scale update rule converge to a local nash equilibrium. *Advances in neural information processing systems*, 30, 2017.
- [29] Hadi Hojjati and Narges Armanfard. Dasvdd: Deep autoencoding support vector data descriptor for anomaly detection. *IEEE Transactions on Knowledge and Data Engineering*, 36(8):3739–3750, 2023.
- [30] Eric Jang, Shixiang Gu, and Ben Poole. Categorical reparameterization with gumbel-softmax. *arXiv preprint arXiv:1611.01144*, 2016.
- [31] Jongheon Jeong, Yang Zou, Taewan Kim, Dongqing Zhang, Avinash Ravichandran, and Onkar Dabeer. Winclip: Zero-/few-shot anomaly classification and segmentation. In *Proceedings of the IEEE/CVF Conference on Computer Vision and Pattern Recognition*, pages 19606–19616, 2023.

- [32] Debesh Jha, Pia H Smedsrud, Michael A Riegler, Pal Halvorsen, Thomas De Lange, Dag Johansen, and Harvard D Johansen. Kvasir-seg: A segmented polyp dataset. In *MultiMedia modeling: 26th international conference, MMM 2020, Daejeon, South Korea, January 5–8, 2020, proceedings, part II* 26, pages 451–462. Springer, 2020.
- [33] Menglin Jia, Luming Tang, Bor-Chun Chen, Claire Cardie, Serge Belongie, Bharath Hariharan, and Ser-Nam Lim. Visual prompt tuning. In *European conference on computer vision*, pages 709–727. Springer, 2022.
- [34] Pranita Balaji Kanade and P. P. Gumaste. Brain tumor detection using mri images, 2015.
- [35] Ali Karami, Thi Kieu Khanh Ho, and Narges Armanfard. Graph-jigsaw conditioned diffusion model for skeleton-based video anomaly detection. In *2025 IEEE/CVF Winter Conference on Applications of Computer Vision (WACV)*, pages 4237–4247. IEEE, 2025.
- [36] Muhammad Uzair Khattak, Hanoona Rasheed, Muhammad Maaz, Salman Khan, and Fahad Shahbaz Khan. Maple: Multi-modal prompt learning. In *Proceedings of the IEEE/CVF conference on computer vision and pattern recognition*, pages 19113–19122, 2023.
- [37] F.C. Kitamura. Headct-hemorrhage. <https://www.kaggle.com/dsv/152137>, 2018.
- [38] Thomas Lai, Thi Kieu Khanh Ho, and Narges Armanfard. Open-set multivariate time-series anomaly detection. *arXiv preprint arXiv:2310.12294*, 2023.
- [39] Chun-Liang Li, Kihyuk Sohn, Jinsung Yoon, and Tomas Pfister. Cutpaste: Self-supervised learning for anomaly detection and localization. In *Proceedings of the IEEE/CVF conference on computer vision and pattern recognition*, pages 9664–9674, 2021.
- [40] Xiang Lisa Li and Percy Liang. Prefix-tuning: Optimizing continuous prompts for generation. *arXiv preprint arXiv:2101.00190*, 2021.
- [41] Jian Liang, Dapeng Hu, and Jiashi Feng. Do we really need to access the source data? source hypothesis transfer for unsupervised domain adaptation. In *International conference on machine learning*, pages 6028–6039. PMLR, 2020.
- [42] Jian Liang, Ran He, and Tieniu Tan. A comprehensive survey on test-time adaptation under distribution shifts. *International Journal of Computer Vision*, 133(1):31–64, 2025.
- [43] Hyesu Lim, Byeonggeun Kim, Jaegul Choo, and Sungha Choi. Ttn: A domain-shift aware batch normalization in test-time adaptation. *arXiv preprint arXiv:2302.05155*, 2023.
- [44] Tsung-Yi Lin, Priya Goyal, Ross Girshick, Kaiming He, and Piotr Dollár. Focal loss for dense object detection. In *Proceedings of the IEEE international conference on computer vision*, pages 2980–2988, 2017.

- [45] Yuejiang Liu, Parth Kothari, Bastien Van Delft, Baptiste Bellot-Gurlet, Taylor Mor-dan, and Alexandre Alahi. Ttt++: When does self-supervised test-time training fail or thrive? *Advances in Neural Information Processing Systems*, 34:21808–21820, 2021.
- [46] Aldo Marzullo and Marta Bianca Maria Ranzini. Exploring zero-shot anomaly detec-tion with clip in medical imaging: Are we there yet? *arXiv preprint arXiv:2411.09310*, 2024.
- [47] Frank J Massey Jr. The kolmogorov-smirnov test for goodness of fit. *Journal of the American statistical Association*, 46(253):68–78, 1951.
- [48] Pankaj Mishra, Riccardo Verk, Daniele Fornasier, Claudio Piciarelli, and Gian Luca Foresti. Vt-adl: A vision transformer network for image anomaly detection and local-ization. In *2021 IEEE 30th International Symposium on Industrial Electronics (ISIE)*, pages 01–06. IEEE, 2021.
- [49] Zachary Nado, Shreyas Padhy, D Sculley, Alexander D’Amour, Balaji Lakshmi-narayanan, and Jasper Snoek. Evaluating prediction-time batch normalization for ro-bustness under covariate shift. *arXiv preprint arXiv:2006.10963*, 2020.
- [50] Ben Peters, Vlad Niculae, and André F. T. Martins. Sparse sequence-to-sequence models. In Anna Korhonen, David Traum, and Lluís Màrquez, editors, *Proceedings of the 57th Annual Meeting of the Association for Computational Linguistics*, pages 1504–1519, Florence, Italy, July 2019. Association for Computational Linguistics. doi: 10.18653/v1/P19-1146. URL <https://aclanthology.org/P19-1146/>.
- [51] Alec Radford, Jong Wook Kim, Chris Hallacy, Aditya Ramesh, Gabriel Goh, Sandhini Agarwal, Girish Sastry, Amanda Askell, Pamela Mishkin, Jack Clark, et al. Learning transferable visual models from natural language supervision. In *International confer-ence on machine learning*, pages 8748–8763. PmLR, 2021.
- [52] Karsten Roth, Latha Pemula, Joaquin Zepeda, Bernhard Schölkopf, Thomas Brox, and Peter Gehler. Towards total recall in industrial anomaly detection. In *Proceedings of the IEEE/CVF conference on computer vision and pattern recognition*, pages 14318–14328, 2022.
- [53] Steffen Schneider, Evgenia Rusak, Luisa Eck, Oliver Bringmann, Wieland Brendel, and Matthias Bethge. Improving robustness against common corruptions by covariate shift adaptation. *Advances in neural information processing systems*, 33:11539–11551, 2020.
- [54] Carole H Sudre, Wenqi Li, Tom Vercauteren, Sebastien Ourselin, and M Jorge Car-doso. Generalised dice overlap as a deep learning loss function for highly unbalanced segmentations. In *Deep Learning in Medical Image Analysis and Multimodal Learn-ing for Clinical Decision Support: Third International Workshop, DLMIA 2017, and 7th International Workshop, ML-CDS 2017, Held in Conjunction with MICCAI 2017, Québec City, QC, Canada, September 14, Proceedings 3*, pages 240–248. Springer, 2017.
- [55] Yu Sun, Xiaolong Wang, Zhuang Liu, John Miller, Alexei Efros, and Moritz Hardt. Test-time training with self-supervision for generalization under distribution shifts. In *International conference on machine learning*, pages 9229–9248. PMLR, 2020.

- [56] Domen Tabernik, Samo Sela, Jure Skvarc, and Danijel Skocaj. Segmentation-based deep-learning approach for surface-defect detection. *Journal of Intelligent Manufacturing*, 31(3):759–776, 2020.
- [57] Nima Tajbakhsh, Suryakanth R Gurudu, and Jianming Liang. Automated polyp detection in colonoscopy videos using shape and context information. *IEEE transactions on medical imaging*, 35(2):630–644, 2015.
- [58] Dequan Wang, Evan Shelhamer, Shaoteng Liu, Bruno Olshausen, and Trevor Darrell. Tent: Fully test-time adaptation by entropy minimization. *arXiv preprint arXiv:2006.10726*, 2020.
- [59] Matthias Wieler and Tobias Hahn. Weakly supervised learning for industrial optical inspection. In *DAGM symposium in*, volume 6, page 11, 2007.
- [60] Min Yang, Dongliang He, Miao Fan, Baorong Shi, Xuetong Xue, Fu Li, Errui Ding, and Jizhou Huang. Dolg: Single-stage image retrieval with deep orthogonal fusion of local and global features. In *Proceedings of the IEEE/CVF International conference on Computer Vision*, pages 11772–11781, 2021.
- [61] Kaiyang Zhou, Jingkang Yang, Chen Change Loy, and Ziwei Liu. Conditional prompt learning for vision-language models. In *Proceedings of the IEEE/CVF conference on computer vision and pattern recognition*, pages 16816–16825, 2022.
- [62] Kaiyang Zhou, Jingkang Yang, Chen Change Loy, and Ziwei Liu. Learning to prompt for vision-language models. *International Journal of Computer Vision*, 130(9):2337–2348, 2022.
- [63] Qihang Zhou, Guansong Pang, Yu Tian, Shibo He, and Jiming Chen. AnomalyCLIP: Object-agnostic prompt learning for zero-shot anomaly detection. In *The Twelfth International Conference on Learning Representations*, 2024. URL <https://openreview.net/forum?id=buC4E91xZE>.
- [64] Yang Zou, Jongheon Jeong, Latha Pemula, Dongqing Zhang, and Onkar Dabeer. Spot-the-difference self-supervised pre-training for anomaly detection and segmentation. In *European Conference on Computer Vision*, pages 392–408. Springer, 2022.

APPENDIX

This appendix provides supplementary details for the BMVC 2025 paper titled "Zero-Shot Anomaly Detection with Dual-Branch Prompt Selection".

- Appendix A provides a comprehensive reviews of related works.
- Appendix B reviews all datasets.
- Appendix C provides information on the baseline methods.
- Appendix D details implementation specifics.
- Appendix E presents additional ablation studies for PILOT.
- Appendix F presents a cross-dataset analysis of prompt diversity and semantics.
- Appendix G reports medical localization results without TTA.
- Appendix H provides a computational analysis of PILOT compared to existing baselines.
- Appendix I compares AnovL with its TTA strategy.
- Appendix J describes the construction of the attribute memory bank.
- Appendix K provides the pseudo code for PILOT.
- Appendix L shows qualitative visualizations of anomaly localization.

A Related Work

Zero-shot Anomaly Detection. ZSAD has gained increasing attention as a solution for identifying anomalies in unseen categories without requiring task-specific training data [10, 31]. Leveraging the generalization capabilities of Vision–Language Models (VLMs) such as CLIP [5], many approaches extend these models by linking image features to textual descriptions of normal and anomalous states. For instance, CLIP-AD [15] and ZOC [14] are early studies that leverage CLIP for ZSAD, but primarily focus on anomaly classification rather than localization. WinCLIP [3] uses multiple handcrafted prompts with iterative patch-based forward passes, and April-GAN [14] refines local semantics via fine-tuning on an auxiliary dataset; both methods address image-level anomaly detection and pixel-level localization. More recent prompt learning methods, such as AnomalyCLIP [6], AnomalyGPT [7], and AdaCLIP [1], optimize object-agnostic text prompts in a single pass using auxiliary dataset. However, reliance on auxiliary datasets may introduce bias and compromise the intended zero-shot setting. This trade-off has been examined by Marzullo et al. [4], who observed that while avoiding auxiliary data reduces fine-tuning overhead, static prompts often fail to adapt to domain shifts; conversely, fine-tuning on auxiliary sets can improve accuracy but risks dataset bias and reduced generalization. Our work aims at addressing these challenges by introducing a dual-branch prompt learning mechanism that combines learnable and fixed prompts, enabling more robust and adaptive anomaly detection under domain shift.

CLIP Adaptation. Recent advances in CLIP fine-tuning primarily rely on prompt learning, in which learnable tokens are introduced into the text encoder to align visual features with related semantics [62]. Approaches such as CoCoOp [60] and visual prompt tuning [83] condition the prompts on image content to improve robustness under domain shift. MaPLe [66] extends prompt learning by inserting learnable tokens into both the visual and text encoders of CLIP, jointly optimizing them to enhance cross-modal alignment. These techniques achieve parameter-efficient adaptation by updating only the prompt representations and, in some cases, only CLIP’s final visual projection layer [22]. Following this rationale, our method fine-tunes the visual projection layer to minimize additional parameters.

Test Time Adaptation. A related direction for adapting CLIP-based models, particularly under domain shift, is TTA. In TTA, the model updates its parameters using unlabeled test data, often guided by pseudo-labels or self-supervised objectives. For instance, self-supervised losses based on the model’s own outputs can fine-tune representations without ground-truth labels [59], and momentum-based pseudo-labeling helps enforce consistency across different augmented views [24]. Other TTA strategies include entropy minimization, which guides the model to assign higher confidence to its predictions on unlabeled data, and the online updating of batch normalization statistics, which helps the model better align with the target distribution during test time. These approaches have been shown to improve robustness and generalization in image classification [49] and segmentation [17]. However, recent studies have found that these techniques are often less effective when the domain shift is large or when the model relies on strong vision-language priors, as in the case of CLIP. To our knowledge, AnovL [119] is the only TTA method for zero-shot anomaly localization, which employs an adapter module for pixel-level refinement and thus introduces additional parameters while focusing solely on localization. In contrast, our method adaptively updates the relevant learnable prompts, incurring no additional parameters and delivering consistent improvements in both image-level anomaly detection and pixel-level anomaly localization.

B Dataset

B.1 Benchmark Datasets

Appendix B provides a comprehensive review of the thirteen benchmark datasets utilized in our study, as summarized in Table 4. To rigorously evaluate both image-level detection and pixel-level localization capabilities of PILOT, we select six industrial inspection datasets. DAGM [69] and DTD-Synthetic [9] comprise textured surfaces exhibiting subtle variations in material appearance, presenting unique challenges for texture-based anomaly detection due to the fine-grained and ambiguous nature of defects. In contrast, MVTec AD [9], VisA [64], BTAD [48], and SDD [56] focus on object-centric industrial scenarios, with defects such as cracks, scratches, dents, and missing components distributed across everyday manufactured and synthetic objects. These datasets are characterized by diverse object categories and high variability in anomaly manifestation, supporting comprehensive benchmarking of localization and generalization performance.

To assess clinical applicability, we include seven medical imaging benchmarks. Three brain scan datasets, HeadCT [67], BrainMRI [64], and Br35H [7], comprise both healthy and pathological subjects, facilitating binary anomaly classification tasks on volumetric neuroimaging data. These datasets encompass a spectrum of anatomical and pathological variations, thereby enabling evaluation of robustness to inter-patient heterogeneity and rare con-

Table 4: Summary of the 13 public benchmark datasets. “Ind” = Industrial, “Med” = Medical, “Def” = Defect detection, “AD” = Anomaly detection, “AL” = Anomaly localization.

Dataset	Cls.	Norm	Anom	Total	Dom.	Task
MVTec AD	15	467	1258	1725	Ind	Def
VisA	12	962	1200	2162	Ind	Def
BTAD	3	451	290	741	Ind	Def
SDD	1	181	74	255	Ind	Def
DAGM	10	6996	1054	8050	Ind	Def
DTD-Synthetic	12	357	947	1304	Ind	Def
HeadCT	1	100	100	200	Med	AD
BrainMRI	1	98	155	253	Med	AD
Br35H	1	1500	1500	3000	Med	AD
ISIC	1	0	379	379	Med	AL
CVC-ClinicDB	1	0	612	612	Med	AL
CVC-ColonDB	1	0	380	380	Med	AL
Kvasir	1	0	1000	1000	Med	AL

ditions. The remaining four datasets provide pixel-wise lesion annotations and consist exclusively of abnormal samples. ISIC [16] features dermoscopic images annotated for skin lesions, while CVC-ClinicDB [6], CVC-ColonDB [57], and Kvasir [32] contain endoscopic images of the gastrointestinal tract, highlighting a range of polyp and ulcer appearances. Since these medical localization datasets lack normal examples, test-time adaptation is not performed for them; their localization results without TTA are reported in Appendix G.

B.2 Domain Discrepancy Analysis

To validate that MVTec AD and VisA indeed represent statistically distinct domains suitable for strict zero-shot evaluation, we quantitatively assessed the distributional discrepancy between their CLIP global feature embeddings. Specifically, we employed Maximum Mean Discrepancy (MMD²) [25], Fréchet Inception Distance (FID) [28], and the Kolmogorov–Smirnov (KS) [47] test. Our analysis yielded $\text{MMD}^2 = 0.0328$ (p -value = 0.0099), indicating a significant difference in embedding distributions. The FID score between the two datasets is 51.9, further corroborating a substantial distributional gap. Additionally, the KS test computed across all feature dimensions revealed that the minimum, mean, and maximum p -values are 0, 5.16×10^{-5} , and 0.0329, respectively, suggesting statistically significant differences in nearly every dimension of the embedding space. These results collectively confirm that MVTec AD and VisA are non-overlapping in the learned representation space, thus justifying their use as auxiliary and target datasets in our zero-shot anomaly detection experiments.

C Baseline

In Appendix C, we compare PILOT against six representative zero-shot anomaly detection methods, summarized as follows:

- **SAA** [10]: Relies on a pretrained Grounding DINO to propose candidate anomaly regions, which are then segmented by the Segment Anything Model (SAM) without any additional training.
- **CoCoOp** [51]: Replaces fixed CLIP prompt tokens with learnable context vectors while keeping the backbone frozen. Offers both a shared “unified” prompt and class-specific prompts to adapt flexibly to unseen categories.
- **WinCLIP** [61]: Splits the image into overlapping windows, encodes each via CLIP to produce localized anomaly scores, and aggregates window predictions through an ensemble of token embeddings—improving spatial localization without fine-tuning.
- **APRIL-GAN** [14]: Builds on WinCLIP by refining text prompts for tighter vision–language alignment and injecting lightweight learnable projections into the visual encoder, thereby sharpening anomaly masks while retaining zero-shot generality.
- **AnomalyCLIP** [63]: Learns object-agnostic “normal” and “anomalous” text prompts, then employs a dense patch-to-prompt attention module (DPAM) to align each visual patch embedding with the appropriate prompt for pixel-level localization.
- **AdaCLIP** [11]: Combines static prompts shared across all inputs for coarse adaptation with dynamic, image-conditioned prompts for fine-grained adjustment. Both prompt sets are jointly learned on auxiliary anomaly data to balance detection accuracy and localization precision.

D Implementation Details

D.1 PILOT Details

Appendix D provides full implementation details of PILOT. We implement PILOT atop the open-source CLIP ViT-L/14@336px backbone, freezing all transformer weights except for the final visual-to-joint projection layer, which is jointly optimized alongside our prompt modules. Our learnable prompt pool \mathcal{P} contains $K = 5$ paired prompts that each comprise $L = 12$ learnable vectors for “normal” and “anomalous” semantics, while a fixed attribute memory bank (see Appendix J) provides semantic tokens extracted from structured templates. All images are uniformly resized to 518×518 pixels, and we extract both the [CLS] token x_{cls} and patch embeddings $\{X^{(M)}\}$ at layers 6, 12, 18, and 24 of the CLIP encoder. All prompt embeddings are initialized by sampling from a Gaussian distribution $\mathcal{N}(0, 0.02)$. PILOT is trained for five epochs using AdamW with a base learning rate of 10^{-3} , a batch size of 32. During test-time adaptation, we fix the pseudo-label fraction at $\rho = 0.25$. All experiments are conducted in PyTorch 2.1.0 on a single NVIDIA Ada A5000 GPU with 32 GB of memory.

D.2 Anomaly State Descriptors

The following anomaly state descriptors are used in our nearest-neighbor analysis, as described in Appendix F of the main text. These descriptors were selected to cover a wide range of mechanical, surface, electrical, pressure-related, assembly, and contamination defects:

- **Mechanical damage:** damaged, scratched, cracked, chipped, broken, bent, punctured, fractured, delaminated, weld defect, loose component, misaligned, deformed, twisted, buckled
- **Surface & corrosion:** rusty, corroded, oxidized, pitted, eroded, paint peeling, stained, contaminated, oil leak, grease smear
- **Thermal & electrical:** overheated, burnt, scorched, melted, short-circuited, electrical arcing, voltage spike damage
- **Sealing & pressure:** leaking, sealing failure, gasket blown, under-pressure, over-pressure, gas leak
- **Wear & fatigue:** worn bearing, surface fatigue crack, abrasion mark, material fatigue, delamination
- **Assembly & alignment:** loose screw, missing bolt, stripped thread, cross-threaded, flange misfit
- **Contamination & blockages:** clogged, blocked channel, foreign particle inclusion, scale buildup, slag inclusion
- **Other:** vibration damage, impact dent, surface blistering, vacuum leak, structural crack

D.3 Entmax_{1.5} Details

Let $\kappa = (\kappa_1, \dots, \kappa_D) \in \mathbb{R}^D$ be a vector of input scores, where each $\kappa_i \in \mathbb{R}$ denotes the unnormalized score for the i -th dimension of interest, and write the probability simplex as

$$\Delta^D = \{\chi \in \mathbb{R}^D \mid \chi_i \geq 0, \sum_{i=1}^D \chi_i = 1\}, \quad (9)$$

where Δ^D is the set of all D -dimensional probability distributions.

The entmax_{1.5} operator produces a sparse probability vector $\chi \in \Delta^D$ via

$$\chi_i = \left[\max(0, \kappa_i - \tau(\kappa)) \right]^2, \quad i = 1, \dots, D, \quad (10)$$

where the scalar $\tau(\kappa) \in \mathbb{R}$ is chosen so that $\sum_{i=1}^D \chi_i = 1$. Intuitively, any entry with $\kappa_i \leq \tau(\kappa)$ is set to zero, and the remaining values are shifted, squared, and renormalized. This yields a differentiable, piecewise-quadratic mapping that retains only the most salient dimensions in its support. In PILOT, injecting Gumbel noise before applying entmax_{1.5} ensures that only the highest-scoring attribute cues survive to influence the final text embedding, providing robust, sparse weighting during training.

E More Ablation Study

E.1 Comparison with SOTA full-shot method

In this comparison, we evaluate PILOT alongside three state-of-the-art fully supervised methods—PatchCore [18], CDO [9], and RD4AD [19]—across six widely used industrial

Table 5: Performance comparison on industrial anomaly detection benchmarks. PILOT is evaluated in the zero-shot setting; all other methods are full-shot. Top section: image-level (AUROC, AP); bottom: pixel-level (AUROC, AUPRO). Best results in bold, second-best underlined.

Industrial Image-level Anomaly Detection (AUROC, AP)				
Dataset	PILOT	PatchCore	CDO	RD4AD
MVTec AD	(92.1, 96.6)	(99.0, 99.7)	(97.1, 97.2)	(<u>98.7</u> , <u>99.4</u>)
VisA	(84.1, 85.7)	(94.6, 95.9)	(<u>95.0</u> , 95.1)	(95.3, 95.7)
BTAD	(<u>95.3</u> , 96.8)	(93.2, 98.6)	(97.6, 97.7)	(93.8, 96.8)
SDD	(87.9, 85.7)	(<u>91.8</u> , <u>91.6</u>)	(96.0, 96.2)	(86.8, 81.3)
DAGM	(98.5, 92.8)	(95.4, 90.3)	(<u>95.1</u> , 95.0)	(92.9, 79.1)
DTD-Synthetic	(97.7, 98.4)	(<u>97.5</u> , <u>97.3</u>)	(96.8, 96.9)	(96.2, 96.3)
Industrial Pixel-level Anomaly Localization (AUROC, AUPRO)				
Dataset	PILOT	PatchCore	CDO	RD4AD
MVTec AD	(90.3, 80.2)	(<u>98.1</u> , 92.8)	(98.2, 98.1)	(97.8, <u>97.6</u>)
VisA	(96.0, 87.2)	(98.5, 92.2)	(99.0, 99.2)	(<u>98.4</u> , <u>98.9</u>)
BTAD	(96.3, 74.9)	(97.4, 74.4)	(98.1, 98.2)	(<u>97.5</u> , <u>97.8</u>)
SDD	(<u>92.4</u> , 73.4)	(87.9, 46.3)	(97.9, 97.7)	(92.2, <u>92.0</u>)
DAGM	(96.0, 91.4)	(95.9, 87.9)	(97.3, 97.2)	(<u>96.8</u> , <u>96.9</u>)
DTD-Synthetic	(98.0, 90.2)	(<u>98.2</u> , <u>98.1</u>)	(98.3, 98.5)	(97.6, 97.7)

benchmarks. Here, a full-shot method refers to a model trained with full access to samples from the target domain. While these baselines leverage direct access to target domain knowledge, PILOT operates solely with pretrained vision–language representations and requires no information from the target domain. Remarkably, PILOT achieves detection accuracy on par with these full-shot models, even when faced with unseen textures or novel defect types. It matches PatchCore’s memory-based robustness, rivals the collaborative feature learning of CDO, and maintains high sensitivity to both global and local irregularities, comparable to RD4AD’s reconstruction-driven approach. However, there remains room for improvement in pixel-level localization accuracy, which we identify as a promising direction for future research. These results underscore the significant potential of zero-shot anomaly detection frameworks in real-world industrial scenarios.

E.2 Pseudo label Statistic

In Table 6 we report three statistics that describe how our TTA selection (See Section 2.5 of the main paper) distributes pseudo-labels over the target dataset D_{tar} . Let $B = |D_{\text{tar}}|$ and recall that we form the top- ρ set A and bottom- ρ set N , with $S = A \cup N$. For each class i in the set of classes \mathcal{I} , we write g_i for the fraction of samples in S belonging to class i .

Table 6: TTA Dataset selection distribution statistics across datasets under different pseudo-labeling ratios ρ . M1: Shannon Evenness, M2: Coefficient of Variation, M3: Percentage of Noisy Label.

Dataset	Class	$\rho=5\%$			$\rho=15\%$			$\rho=25\%$			$\rho=35\%$			$\rho=50\%$		
		M1	M2	M3	M1	M2	M3	M1	M2	M3	M1	M2	M3	M1	M2	M3
MVTec AD	15	0.76	1.21	10.3%	0.97	0.45	8.1%	0.93	0.71	7.8%	0.95	0.59	11.2%	1.00	0.00	27.3%
VisA	12	0.79	0.97	12.0%	0.98	0.27	13.2%	0.98	0.35	14.2%	0.99	0.31	16.1%	1.00	0.00	31.4%
BTAD	3	0.79	0.76	21.6%	0.86	0.70	12.6%	0.93	0.50	17.3%	0.95	0.39	20.4%	1.00	0.00	36.5%
SDD	1	0.72	0.59	0.0%	0.61	0.69	7.6%	0.63	0.68	6.3%	0.74	0.58	10.1%	1.00	0.00	39.6%
DAGM	10	0.73	1.35	3.9%	0.88	0.76	1.3%	0.95	0.56	0.7%	0.97	0.43	0.9%	1.00	0.00	6.9%
DTD-Synthetic	12	0.72	1.34	3.0%	0.96	0.47	6.1%	0.95	0.53	4.6%	0.96	0.48	5.2%	1.00	0.00	20.7%

- **Shannon evenness** E is defined as

$$E = -\frac{\sum_{i \in \mathcal{I}} g_i \ln g_i}{\ln |\mathcal{I}|}.$$

Values near 1 indicate that the selected samples S are spread uniformly across all classes. This is referred as M1 in Table 6.

- **Coefficient of variation** CV is

$$CV = \frac{\sigma(g)}{\mu(g)},$$

where $\mu(g)$ and $\sigma(g)$ are the mean and standard deviation of $\{g_i\}$. A low CV signals a balanced class-wise count. This is referred as M2 in Table 6.

- **Noisy label rate** is the fraction of indices in S whose pseudo-label \tilde{y}_j disagrees with the ground-truth label y_j . This is referred as M3 in Table 6.

As ρ grows, we observe that E increases and CV decreases, confirming that selecting a larger fraction of samples both diversifies class coverage and balances the counts. At the same time, the noisy label rate rises, reflecting the classic trade-off: higher coverage under TTA comes at the expense of pseudo-label accuracy.

E.3 Other TTA Method

To better understand the impact of different TTA strategies on anomaly detection performance, we conduct an ablation study comparing several representative TTA methods. As shown in Table 7, we evaluate TENT [58], BN Adaptation [43], and soft pseudo labeling alongside our proposed PILOT framework.

Table 7: Ablation of different TTA methods on industrial anomaly detection datasets. Metrics reported: Image-level (AUROC, AP) and Pixel-level (AUROC, AUPRO).

TTA Method	Image-level		Pixel-level	
	AUROC	AP	AUROC	AUPRO
TENT	74.3	73.5	61.6	40.9
BN Adaptation	70.5	69.8	55.2	34.5
Soft Pseudo Label	91.0	91.2	92.0	79.8
PILOT	92.6	92.7	94.8	82.9

Table 7 presents the results of different TTA strategies on industrial anomaly detection benchmarks. Both TENT and BN Adaptation exhibit weak performance in this setting, particularly for pixel-level localization, suggesting that these conventional TTA methods are not well suited for adapting CLIP-based models. Recent literature has also observed that methods such as TENT, which adapt only batch normalization parameters, often struggle when applied to models with large distribution shifts or strong vision-language priors, as is the case with CLIP [4]. In contrast, the soft pseudo labeling strategy leads to more stable improvements, although its cautious approach may be less aggressive in leveraging adaptation signals. Our findings suggest that confidence-based pseudo-labeling, as used in the PILOT TTA framework, provides the most effective adaptation and yields the best overall performance in this scenario.

E.4 Effect of Learnable Prompt Pool Size

Table 8: Effect of prompt pool size K on the industrial benchmark. Best in each row is **bold**.

Level	Metric	K								
		2	3	4	5	7	10	16	32	64
Image-level	AUROC	85.9	88.6	91.3	92.6	92.4	92.4	92.9	93.2	91.7
	AP	87.2	90.8	91.9	92.7	92.0	92.0	93.5	93.8	92.2
Pixel-level	AUROC	94.1	93.7	94.6	94.8	91.7	88.0	89.4	87.1	83.7
	AUPRO	82.1	81.0	82.4	82.9	80.9	77.2	78.3	76.3	73.8

Table 8 examines how changing the number of learnable prompts influences performance. As the pool size increases, image-level metrics rise steadily and then level off once a moderate number of prompts is reached, indicating improved anomaly discrimination with greater prompt diversity. However, pixel-level metrics follow a different trend: they increase up to a moderate pool size but then decline with further increases, reflecting reduced generalization for localization. This divergence shows that while a larger pool improves global detection, overly large pools lead to redundancy and overfitting at the pixel level, making a moderate pool size optimal for balancing both objectives.

E.5 Effect of Attribute Memory Bank Size.

Table 9: Effect of attribute-memory bank size C on the industrial benchmark. Best in each row is **bold**.

Level	Metric	C						
		5	25	50	75	100	150	
Image-level	AUROC	88.1	92.1	92.5	92.6	92.7	92.2	
	AP	88.4	92.0	92.4	92.7	92.6	92.3	
Pixel-level	AUROC	87.7	93.9	94.5	94.8	94.6	94.4	
	AUPRO	76.1	82.2	82.7	82.9	82.8	82.5	

Table 9 shows the impact of varying the number of attribute templates. Expanding the memory bank from a small to a moderate size leads to clear improvements in both image-level and pixel-level performance, as the model benefits from richer semantic information. Beyond this range, image-level metrics stabilize, while pixel-level gains plateau and may slightly decrease with the largest banks. This suggests that adding more attributes beyond a

certain point does not further improve generalization, and that a compact but diverse attribute bank is sufficient to provide strong semantic guidance.

E.6 Effect of ρ fraction

Table 10: Effect of pseudo-label fraction ρ (%) during TTA (industrial datasets). Best value in each column is **bold**.

Level	Metric	ρ (%)				
		5	15	25	35	50
Image-level	AUROC	92.4	93.0	92.6	90.1	88.5
	AP	92.5	93.1	92.7	90.2	88.7
Pixel-level	AUROC	92.4	93.6	94.8	92.7	91.5
	AUPRO	81.0	81.9	82.9	79.9	78.0

We vary the pseudo-label fraction ρ during TTA, as shown in Table 10. Using a small set of high-confidence pseudo labels leads to improvements in image-level performance compared to no adaptation, as the adaptation process focuses on the most reliable samples. Notably, pixel-level performance remains largely unchanged when only a small subset is used, but begins to improve as ρ increases to an intermediate fraction. At this optimal point, the model is able to leverage a greater diversity of anomaly patterns without introducing substantial label noise. Beyond this, further increases in ρ admit less reliable pseudo labels, resulting in a sharp decline in both detection and localization metrics.

E.7 Prompt Aggregation Ablation

Table 11: Ablation for prompt aggregation. “w/o TTA” and “w/ TTA” indicate performance without and with TTA, respectively. “Extra” indicates whether additional trainable parameters are used. OP: orthogonal projector as used in PILOT; GF: Gate Fusion [8]; CA: Cross Attention [13].

Proj.	Extra	Image		Pixel	
		w/o TTA	w/ TTA	w/o TTA	w/ TTA
GF	✓	(91.2, 90.0)	(91.5, 90.8↑)	(88.6, 77.8)	(89.4↑, 77.6○)
CA	✓	(92.1, 92.4)	(93.1↑, 92.9↑)	(93.7, 81.3)	(86.4↓, 75.3↓)
OP	×	(90.3, 91.1)	(92.6↑, 92.7↑)	(93.5, 81.5)	(94.8↑, 82.9↑)

Table 11 compares three prompt aggregation strategies and reveals that methods like Gate Fusion [8] and Cross Attention [13], while capable of improving image-level anomaly detection, tend to destabilize pixel-level localization during TTA. While these approaches may leverage the attribute memory bank as a semantic anchor, their extra parameters are directly updated using noisy pseudo-labels and only image-level supervision. This makes them prone to parameter drift, which can erode the stability needed for precise localization under domain shift. In contrast, the orthogonal projector used in PILOT achieves reliable gains across both detection and localization tasks without introducing extra parameters, as it keeps the attribute embedding fixed as a semantic reference and allows only the prompt representation to adapt. This encourages adaptation in directions that are truly complementary, while avoiding redundancy and overfitting.

E.8 Effect of Orthogonal Projection

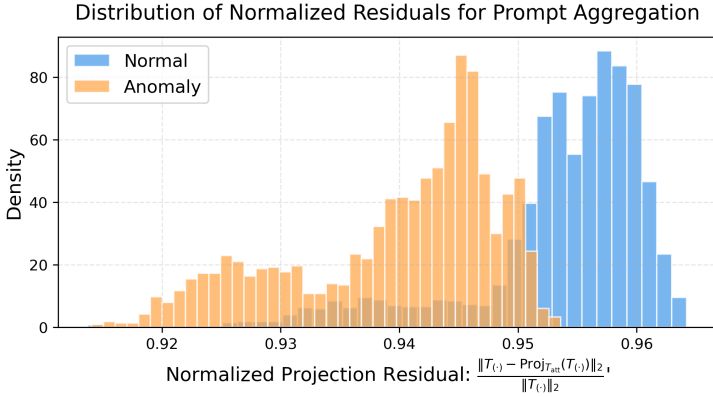


Figure 2: Histogram of normalized projection residuals for normal and anomaly prompts (see Eq. 5). The y-axis shows the fraction of samples per bin. Higher values indicate greater orthogonality to the anchor, while lower values reflect stronger alignment.

To evaluate the effectiveness of our orthogonal projection strategy for prompt aggregation (Equation 5), we analyze the distribution of normalized projection residuals defined as:

$$\frac{\|T_{(.)} - \text{Proj}_{T_{\text{att}}}(T_{(.)})\|_2}{\|T_{(.)}\|_2} \quad (11)$$

for both learnable prompts T_n (normal) and T_a (anomaly), as shown in Figure 2. The resulting histograms exhibit consistently nonzero residuals, which are clearly separated between normal and anomalous samples. This indicates that the learnable prompts encode substantial information complementary to the attribute embedding T_{att} , rather than merely duplicating its semantics. Notably, anomalous prompts display larger orthogonal components, highlighting the model’s ability to leverage diverse information captured by the learnable prompts. Empirically, these findings confirm that the orthogonal projection mechanism extracts and integrates useful, non-redundant cues into the fused embedding, thereby validating our parameter-free aggregation approach.

F Prompt Diversity

To examine the diversity within our learnable prompt pool \mathcal{P} , we analyzed pairwise relationships among the learned prompt embeddings across multiple industrial datasets. Specifically, we measured the pairwise cosine similarity between prompt embeddings within each dataset. Figure 3(a) summarizes these findings using boxplots. The results demonstrate consistent diversity across all evaluated datasets, with median similarity values generally below 0.5, indicating that the learned prompts capture distinct representations.

To further understand how this diversity is practically leveraged, Figure 3(b) illustrates the relative contributions of each prompt in the pool across multiple datasets. The observed variations suggest that rather than relying on a single dominant prompt, the model adaptively emphasizes different prompts based on specific dataset characteristics. This adaptive

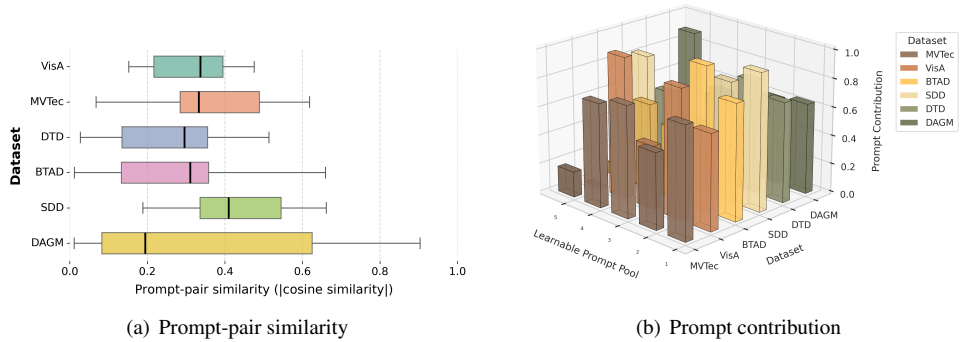


Figure 3: (a) Prompt-pair similarity distributions: each horizontal boxplot shows absolute cosine similarity between learned prompt embeddings. Values close to 0 indicate high diversity. (b) Prompt contribution: normalized contribution of a learnable prompt from the pool \mathcal{P} , aggregated over test images. Higher values indicate greater involvement during TTA.

utilization indicates that the prompt pool effectively leverages its inherent diversity to accommodate the varying requirements of different anomaly detection scenarios.

Table 12: Top-3 anomaly state matches for each learned prompt on the VisA dataset, retrieved via FAISS nearest neighbor search between the prompt embedding and the CLIP text embedding of “a photo of a [anomaly state] object”. For each prompt, \circ indicates matches after finetuning on the auxiliary set (\mathcal{D}_{aux}), and \bullet indicates matches after TTA on the target set (\mathcal{D}_{tar}). The top-3 matches are listed in descending order of cosine similarity.

Prompt	Top-3 Matches
1	\circ misaligned, bent, over-pressure \bullet bent, misaligned, flange misfit
2	\circ abrasion mark, delamination, oxidized \bullet bent, flange misfit, clogged
3	\circ damaged, corroded, weld defect \bullet damaged, impact dent, eroded
4	\circ damaged, cracked, weld defect \bullet damaged, voltage spike damage, weld defect
5	\circ damaged, paint peeling, weld defect \bullet damaged, voltage spike damage, contaminated

Having established the inherent diversity within our learnable prompt pool \mathcal{P} , we further investigated how this diversity corresponds to meaningful anomaly characteristics expressed in natural language. To accomplish this, we conducted a nearest-neighbor analysis using FAISS [20], comparing anomaly prompt embeddings (T_a) to embeddings generated from textual templates of the form “a photo of a [anomaly state] object.” Various anomaly state descriptors were used to represent potential real-world anomalies.

Table 12 lists the top-3 nearest textual descriptors for each prompt embedding, both

before and after TTA. Additional results are provided in Appendix G. Prompts were initially trained on the MVTec auxiliary set and subsequently adapted to the VisA target set. The nearest-neighbor analysis revealed clear and meaningful alignments between the learned prompts and natural language anomaly descriptors. Prompts originally associated with anomaly states such as “misaligned,” “bent,” or “eroded” consistently maintained these semantic associations after adaptation, showing subtle shifts that reflect nuances in the target dataset. These observations underscore that the diversity within our learned prompt pool corresponds meaningfully to recognizable natural-language concepts.

Table 13: Top-3 anomaly state matches for each learned prompt (1–5) on six datasets. Ranks are indicated by ①, ②, and ③. Each match is the closest to the template “a photo of a [anomaly state] object”.

Prompt	MVTec AD	VisA	BTAD	SDD	DAGM	DTD-Synthetic
1	① rusty ② abrasion mark ③ flange misfit	① bent ② misaligned ③ flange misfit	① over-heated ② short-circuited ③ misaligned	① bent ② misaligned ③ electrical arcing	① bent ② eroded ③ electrical arcing	① delamination ② under-pressure ③ over-pressure
2	① punctured ② electrical arcing ③ short-circuited	① bent ② flange misfit ③ clogged	① abrasion mark ② weld defect ③ surface blistering	① abrasion mark ② chipped ③ weld defect	① abrasion mark ② grease smear ③ chipped	① electrical arcing ② delamination ③ under-pressure
3	① damaged ② impact dent ③ cracked	① damaged ② impact dent ③ eroded	① damaged ② weld defect ③ abrasion mark	① damaged ② abrasion mark ③ scratched	① surface fatigue crack ② grease smear ③ scratched	① damaged ② short-circuited ③ eroded
4	① bent ② gasket blown ③ cross-threaded	① damaged ② voltage spike damage ③ weld defect	① damaged ② cracked ③ broken	① weld defect ② surface fatigue crack ③ damaged	① surface fatigue crack ② cracked ③ damaged	① cracked ② damaged ③ broken
5	① scratched ② grease smear ③ over-heated	① damaged ② voltage spike damage ③ contaminated	① damaged ② weld defect ③ abrasion mark	① weld defect ② damaged ③ surface fatigue crack	① surface fatigue crack ② structural crack ③ weld defect	① surface fatigue crack ② grease smear ③ structural crack

Table 13 further extends this semantic exploration, reporting the top-3 nearest textual matches for each learned prompt (1–5) across all six industrial anomaly detection datasets. Each match is derived from the template “a photo of a [anomaly state] object.”

This broader analysis underscores that individual prompts exhibit varying associations with different anomaly states depending on the dataset. Such variability demonstrates the model’s capacity to adapt prompt representations across diverse domains. While some semantic associations remain stable, others shift considerably, reflecting both shared and domain-specific semantic cues. Collectively, these findings reinforce the effectiveness of our

prompt pool in capturing diverse anomaly characteristics and adapting its semantic emphasis in response to domain-specific features.

G Medical anomaly localization results

Table 14: Comparison of model performance on medical anomaly localization datasets. Pixel-level results (AUROC, AUPRO) in parentheses. Best entries are marked with bold and second-best entries with underline.

Medical Pixel-level Anomaly Localization (AUROC, AUPRO)							
Dataset	SAA	CoCoOp	WinCLIP	APRIL-GAN	AnomalyCLIP	AdaCLIP	PILOT w/o TTA
ISIC	(83.8, 74.2)	(51.7, 15.9)	(83.3, 55.1)	(89.4, 77.2)	(87.4, <u>74.5</u>)	(84.4, 54.5)	(<u>87.8</u> , 74.2)
CVC-ColonDB	(71.8, 31.5)	(40.5, 2.6)	(70.3, 32.5)	(78.4, 64.6)	(88.5, 79.3)	(88.0, 63.9)	(88.6, 78.2)
CVC-ClinicDB	(66.2, 29.1)	(34.8, 2.4)	(51.2, 13.8)	(80.5, 60.7)	(93.0, 81.6)	(94.4, 73.5)	(92.1, <u>78.5</u>)
Kvasir	(45.9, 13.3)	(44.1, 3.5)	(69.7, 24.5)	(75.0, 36.2)	(93.2, 59.9)	(94.6, 26.2)	(<u>94.0</u> , <u>58.8</u>)
Mean	(66.9, 37.0)	(42.8, 6.1)	(68.6, 31.5)	(80.8, 59.7)	(90.5, 73.8)	(90.4, 54.5)	(90.6, 72.4)

Medical anomaly localization results are reported in Table 14, with all evaluations conducted without TTA. Since medical datasets lack explicit “normal” examples, our TTA strategy cannot be applied; nevertheless, PILOT still produces competitive localization maps, achieving the highest mean AUROC and the second-best AUPRO across benchmarks. These results underscore the generality of our dual-branch prompt learning framework: even in the absence of adaptation, dynamically weighting prompts with the most relevant anomaly cues deliver state-of-the-art performance in medical domains.

H Computational Analysis

Table 15 compares PILOT against our main competitors, AnomalyCLIP and AdaCLIP, in terms of model size, computational cost, inference speed, and GPU memory footprint. All measurements were obtained on an NVIDIA Ada A5000 GPU, as detailed in Appendix D.1. PILOT exhibits a resource profile closely aligned with AnomalyCLIP, and significantly outperforms AdaCLIP across all measured metrics. Importantly, PILOT employs a two-phase process: during the initial training phase, it utilizes a moderately sized model, while in the TTA phase, only the learnable prompt pool (\mathcal{P}) is updated. By limiting parameter updates to \mathcal{P} during deployment, PILOT further reduces computational requirements, enhancing its practical suitability for near real-time anomaly detection in resource-constrained environments.

Table 15: Comparison of computational resource requirements for PILOT and main competitors. GFLOPs, latency, and GPU memory are reported for the test phase. Trainable parameters are reported for the training phase in all methods; for PILOT, test-time adaptation parameters are also shown (train / test).

Method	Params (M)	GFLOPs	Latency (ms)	GPU Mem (MB)
AnomalyCLIP	5.56	482.06	107.4	2051.7
AdaCLIP	10.67	2872.37	219.0	8752.5
PILOT	6.40 (Train) / 5.61 (Test)	491.39	109.9	2398.4

I Compared with AnovL

AnovL [19] is, to our knowledge, the only existing test-time adaptation method tailored for zero-shot anomaly localization. It introduces a lightweight adapter on the visual token stream and refines pixel-level anomaly maps by minimizing a self-supervised reconstruction loss; the adapter learns to reconstruct features of normal patches, so that anomalous regions, whose reconstructions incur higher error, become more salient.

To investigate the complementarity of these adaptation schemes, we conducted an ablation in which PILOT’s image-level TTA is combined with AnovL’s pixel reconstruction loss (row “+ AnovL Loss”). Although this hybrid approach retains PILOT’s adaptive prompt weighting mechanism and the visual adapter architecture, it failed to improve either localization or detection. This result suggests that the reconstruction and pseudo-label losses impose conflicting objectives on the same prompt parameters, generating contradictory update signals that destabilize adaptation and ultimately degrade performance.

By design, AnovL’s adaptation objective targets only pixel-level refinement and does not update any image-level scoring components. As a result, AnovL achieves modest gains in localization accuracy but has no impact on image-level detection (Table 16). In contrast, PILOT’s TTA strategy optimizes a high-confidence, image-level objective by adaptively updating the learnable prompt parameters according to their relevance for each test image, which leads to consistent improvements on both image- and pixel-level metrics. This dual benefit arises because PILOT emphasizes prompt parameters most aligned with the test data, while the fixed attribute embeddings act as semantic anchors to stabilize adaptation and prevent parameter drift.

To investigate the complementarity of these adaptation schemes, we conducted an ablation in which PILOT’s image-level TTA is combined with AnovL’s pixel reconstruction loss (row “+ AnovL Loss”). Although this hybrid approach retains PILOT’s adaptive prompt weighting mechanism and the visual adapter architecture, it failed to improve either localization or detection. We hypothesize that the reconstruction and pseudo-label losses impose conflicting objectives on the same prompt parameters, driving contradictory update signals that destabilize adaptation and degrade performance.

Table 16: Comparison between PILOT and AnovL on two benchmarks (MVTec AD and VisA). “w/o TTA” and “w/ TTA” indicate performance without and with test-time adaptation, respectively. Arrows denote change under TTA: \uparrow (improvement), \downarrow (decline), \circ (no significant change, ± 0.5).

Method	MVTec AD				VisA			
	Image (AUROC, AP)		Pixel (AUROC, AUPRO)		Image (AUROC, AP)		Pixel (AUROC, AUPRO)	
	w/o TTA	w/ TTA	w/o TTA	w/ TTA	w/o TTA	w/ TTA	w/o TTA	w/ TTA
AnovL	(87.9, 93.8)	(87.9 \circ , 93.8 \circ)	(82.7, 60.2)	(84.8 \uparrow , 68.4 \uparrow)	(72.6, 76.9)	(72.6 \circ , 76.9 \circ)	(84.4, 62.0)	(85.6 \uparrow , 64.1 \uparrow)
PILOT	(90.2, 95.7)	(92.1 \uparrow , 96.6 \uparrow)	(89.4, 79.2)	(90.3 \uparrow , 80.2 \uparrow)	(82.0, 84.1)	(84.1 \uparrow , 85.7 \uparrow)	(94.8, 85.6)	(96.0 \uparrow , 87.2 \uparrow)
+ AnovL Loss	(90.2, 95.7)	(87.5 \downarrow , 89.7 \downarrow)	(89.4, 79.2)	(66.4 \downarrow , 52.3 \downarrow)	(82.0, 84.1)	(73.9 \downarrow , 78.1 \downarrow)	(94.8, 85.6)	(79.4 \downarrow , 65.8 \downarrow)

J Details of Attribute Memory Bank Construction

To construct the attribute memory bank, we first define four fixed sets of text templates, each capturing domain-relevant semantics for anomaly detection. Specifically, two sets encode object states: a normal state set, which contains descriptors such as “normal { }” and “flawless { },” and an anomalous state set, which includes terms like “damaged { }” and “imperfect

{ }.” In addition, we curate three context template lists to capture diverse imaging scenarios: a set for general visual conditions (e.g., “a cropped photo of the { }” or “a blurry photo of a { } for anomaly detection”), an industrial context set (e.g., “an industrial photo of a { }” or “a bright industrial photo of the { }”), and a medical context set (e.g., “a CT scan of a { }” or “an ultrasound image of a { }”).

For each object class, we instantiate all possible combinations by inserting the class name into each entry of the normal and anomalous state sets, and further merging them with every template from the general, industrial, and medical context lists. This combinatorial process results in a comprehensive set of several hundred prompts per class, spanning a wide spectrum of visual conditions and attribute states. For example, for the class “bearing,” we synthesize prompts such as “normal bearing in a cropped photo,” “imperfect bearing in a bright industrial photo,” and “damaged bearing in an ultrasound image.”

All generated prompts are tokenized and encoded using the CLIP text encoder, after which the resulting embeddings are L2-normalized. To facilitate efficient retrieval, the embeddings are partitioned into two disjoint subsets corresponding to normal and anomalous states, thereby enabling the attribute memory bank to provide appropriate semantic vectors during prompt weighting for both image-level and pixel-level anomaly detection tasks. This construction ensures that the memory bank captures a rich and diverse set of attribute semantics, supporting robust prompt weighting and improved generalization to unseen domains.

K Pseudo Code

In Appendix K, we present high-level pseudocode for both the training and test-time adaptation procedures of PILOT. Algorithm 1 details the end-to-end optimization on the auxiliary dataset D_{aux} , where we jointly update the learnable prompt pool \mathcal{P} , attribute memory bank \mathcal{U} , and final visual projection layer using combined image-level and pixel-level objectives. Algorithm 2 then describes our confidence-based, image-level objective TTA scheme on an unlabeled target set D_{tar} , in which only the relevant prompt parameters and their associated r_k, s_k embeddings are fine-tuned to align with high-confidence pseudo-labels.

L Visualization

In this section, we present qualitative examples for a subset of categories from each industrial dataset generated by PILOT. Figures 4-25 illustrate representative images and corresponding anomaly maps; to maintain clarity, we omit exhaustive visualizations of every class.

Algorithm 1 Training Procedure for PILOT

Require: Dataset $D_{aux} = \{(I_i, y_i, G_i)\}$; Learnable Prompt Pool \mathcal{P} ; Attribute Memory Bank \mathcal{U} ; Vision Encoder f_{visual} ; Text Encoder f_{text} ; epochs E ; batch size B

- 1: **Freeze** all weights except: last visual projection, learnable prompt pool, attribute memory bank ▷ initialize model
 - 2: **for** $e = 1$ **to** E **do**
 - 3: **for** each batch (I, y, G) in D_{aux} **do**
 - 4: $x_{cls}, \{X^{(m)}\}_{m \in M} \leftarrow f_{visual}(I)$ ▷ extract global & patch features from the vision encoder
 - 5: $\alpha \leftarrow Q_{lrn}(x_{cls}, \mathcal{P})$
 - 6: $\bar{p}^n, \bar{p}^a \leftarrow \sum_{k=1}^K \alpha_k p_k^n, \sum_{k=1}^K \alpha_k p_k^a$ ▷ aggregate prompts with learned weights
 - 7: $T_n, T_a \leftarrow f_{text}(\bar{p}^n, \bar{p}^a)$ ▷ encode normal/anomaly prompt
 - 8:
 - 9: $\beta \leftarrow Q_{att}(x_{cls}, \mathcal{U})$
 - 10: initial Gumbel noise
 - 11: $\phi_c \leftarrow \text{entmax}_{1.5}(\beta_c + \text{noise})$ ▷ ensure sparsity
 - 12: $T_{att} \leftarrow \sum_{c=1}^C \phi_c u_c$ ▷ construct attribute representation
 - 13:
 - 14: $T_n^{fus}, T_a^{fus} \leftarrow \text{Projector}(T_{att}, T_n, T_a)$ ▷ fuse by projector
 - 15: $\hat{y} = \sigma(\text{sim}(x_{cls}, T_{(\cdot)}^{fus}))$ ▷ image-level score
 - 16: $\mathcal{L}_{\text{image}} = \text{BCE}(\hat{y}, y)$ ▷ image-level loss
 - 17: **for** each $m \in M$ **do**
 - 18: $\hat{G}^{(m)} = \sigma(\text{sim}(X^{(m)}, T_{(\cdot)}^{fus}))$ ▷ pixel anomaly map
 - 19: **end for**
 - 20: $\mathcal{L}_{\text{pixel}} = \frac{1}{|M|} \sum_{m \in M} [\text{Focal}(\hat{G}^{(m)}, G) + \text{Dice}(\hat{G}^{(m)}, G)]$ ▷ pixel-level loss
 - 21: $\mathcal{L}_{\text{PILOT}} = \mathcal{L}_{\text{image}} + \mathcal{L}_{\text{pixel}}$ ▷ total loss
 - 22: **Update** prompt pool, attribute bank, projection using $\mathcal{L}_{\text{PILOT}}$
 - 23: **end for**
 - 24: **end for**
-

Algorithm 2 Test-Time Adaptation Procedure for PILOT

Require: Target dataset $D_{tar} = \{I_t\}$; Trained model (f_{visual} , f_{text} , prompt pool \mathcal{P} , attribute bank \mathcal{U}); confidence fraction ρ ; epochs E

- 1: **Freeze** all weights except selected prompt(s) and associated selector/prototype embeddings
- 2: **for** $e = 1$ **to** E **do**
- 3: **for** each I_t in D_{tar} **do**
- 4: $x_{cls}^t \leftarrow f_{visual}(I)$ ▷ extract global features
- 5: $\bar{p}^n, \bar{p}^a \leftarrow \sum_{k=1}^K \alpha_k p_k^n, \sum_{k=1}^K \alpha_k p_k^a$ ▷ aggregate prompts with learned weights
- 6: $T_n, T_a \leftarrow f_{text}(\bar{p}^n, \bar{p}^a)$ ▷ encode normal/anomaly prompt
- 7: $\beta \leftarrow Q_{att}(x_{cls}, \mathcal{U})$
- 8: initial Gumbel noise
- 9: $\phi_c \leftarrow \text{entmax}_{1.5}(\beta_c + \text{noise})$ ▷ ensure sparsity
- 10: $T_{att} \leftarrow \sum_{c=1}^C \phi_c u_c$ ▷ construct attribute representation
- 11: $T_n^{fus}, T_a^{fus} \leftarrow \text{Projector}(T_{att}, T_n, T_a)$ ▷ fuse by projector
- 12: $\tilde{y} = \sigma(\text{sim}(x_{cls}^t, T_{(\cdot)}^{fus}))$ ▷ image-level anomaly score
- 13: **end for**
- 14: Collect all scores $\{\tilde{y}_i\}_{i=1}^{|D_{tar}|}$
- 15: Identify top/bottom ρ -fraction: $A = \text{Top}_k\{\tilde{y}_i\}$, $N = \text{Bot}_k\{\tilde{y}_i\}$, $k = \lceil \rho |D_{tar}| \rceil$
- 16: Assign pseudo-labels: $\tilde{y}_i = 1$ if $i \in A$, $\tilde{y}_i = 0$ if $i \in N$
- 17: $\mathcal{L}_{image}^{TTA} = \frac{1}{|A|+|N|} \sum_{i \in A \cup N} \text{BCE}(\tilde{y}_i, \text{pseudo-labels})$ ▷ image-level TTA loss
- 18: **Update** only the prompt(s) and associated embedding relevant to the current input to minimize $\mathcal{L}_{image}^{TTA}$
- 19: **end for**

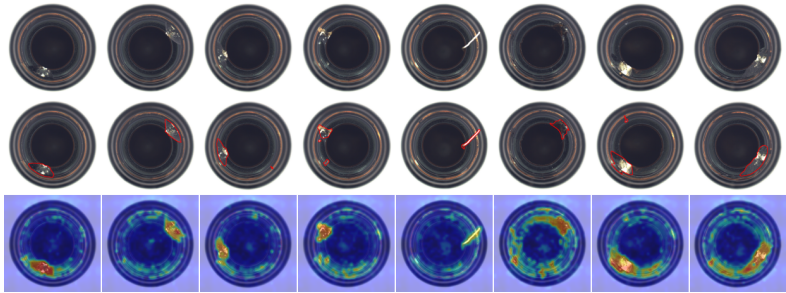


Figure 4: Visualization of input images (top), ground-truth masks (middle), and model-generated anomaly maps (bottom) for the *bottle* category in the MVTec AD dataset. All results are generated by PILOT.

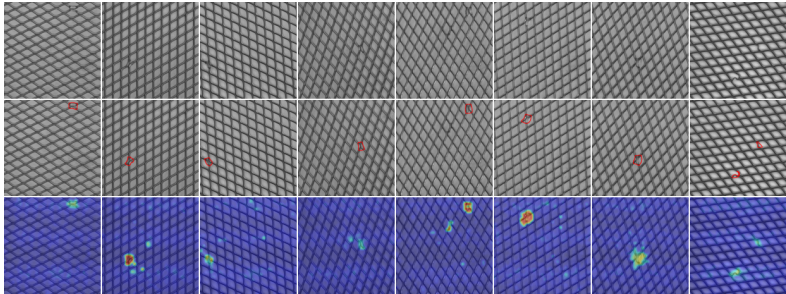


Figure 5: Visualization of input images (top), ground-truth masks (middle), and model-generated anomaly maps (bottom) for the *grid* category in the MVTec AD dataset. All results are generated by PILOT.

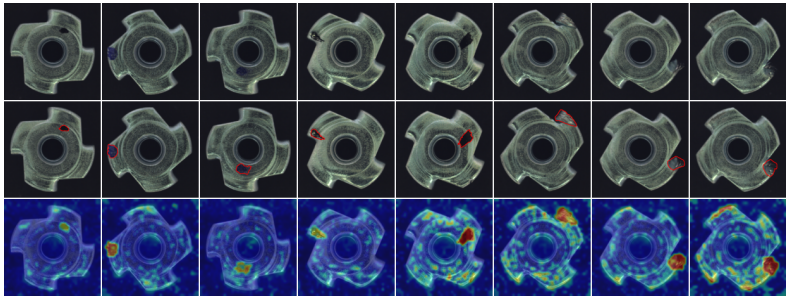


Figure 6: Visualization of input images (top), ground-truth masks (middle), and model-generated anomaly maps (bottom) for the *metal nut* category in the MVTec AD dataset. All results are generated by PILOT.

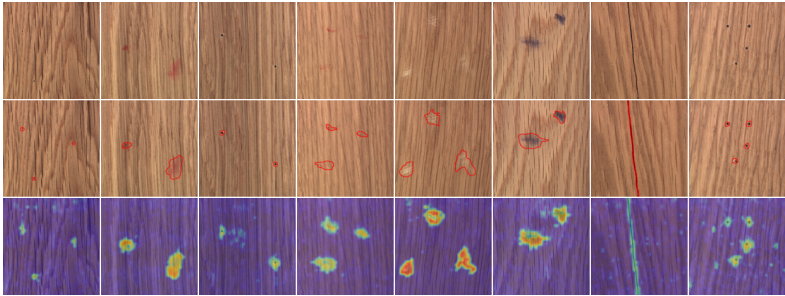


Figure 7: Visualization of input images (top), ground-truth masks (middle), and model-generated anomaly maps (bottom) for the *wood* category in the MVTec AD dataset. All results are generated by PILOT.

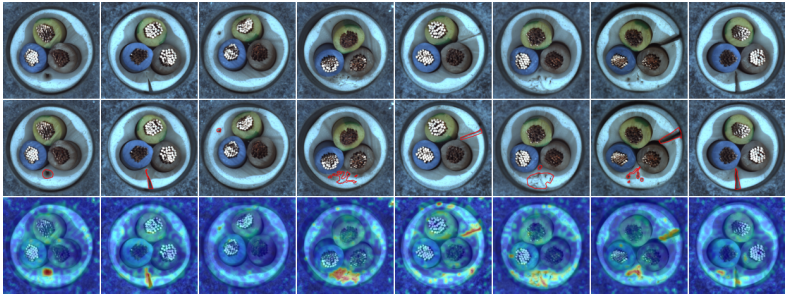


Figure 8: Visualization of input images (top), ground-truth masks (middle), and model-generated anomaly maps (bottom) for the *cable* category in the MVTec AD dataset. All results are generated by PILOT.

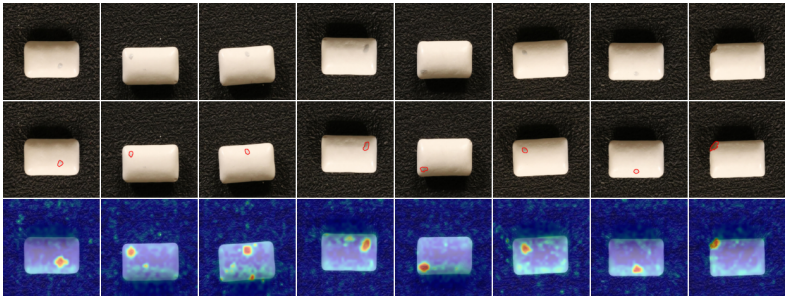


Figure 9: Visualization of input images (top), ground-truth masks (middle), and model-generated anomaly maps (bottom) for the *chewinggum* category in the VisA dataset. All results are generated by PILOT.

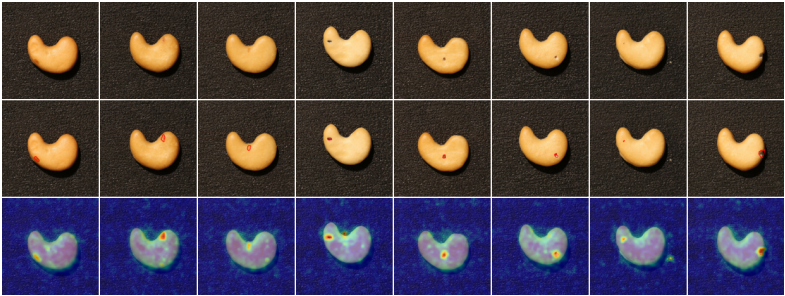


Figure 10: Visualization of input images (top), ground-truth masks (middle), and model-generated anomaly maps (bottom) for the *cashew* category in the VisA dataset. All results are generated by PILOT.

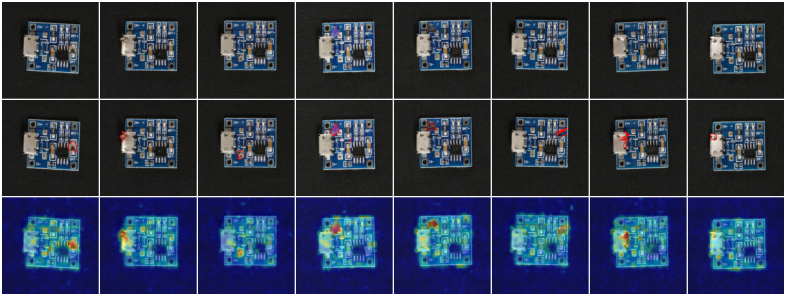


Figure 11: Visualization of input images (top), ground-truth masks (middle), and model-generated anomaly maps (bottom) for the *pcb4* category in the VisA dataset. All results are generated by PILOT.

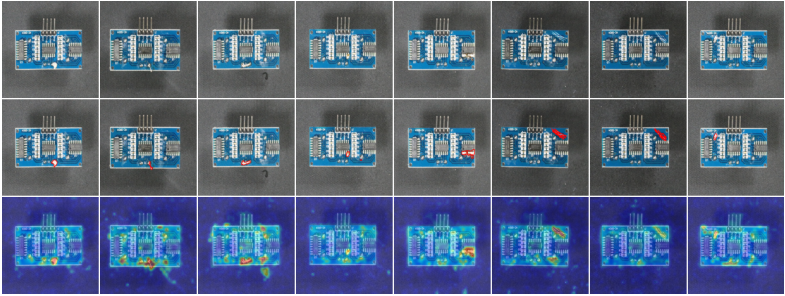


Figure 12: Visualization of input images (top), ground-truth masks (middle), and model-generated anomaly maps (bottom) for the *pcb2* category in the VisA dataset. All results are generated by PILOT.

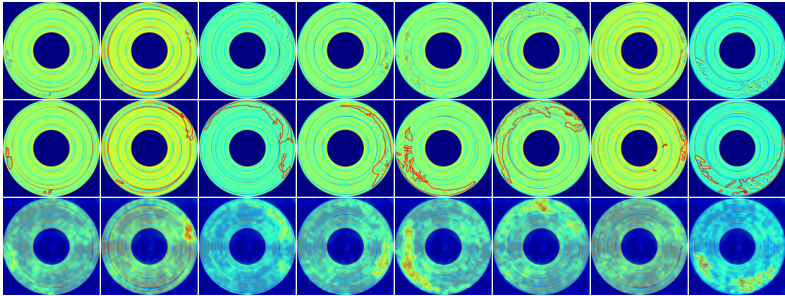


Figure 13: Visualization of input images (top), ground-truth masks (middle), and model-generated anomaly maps (bottom) for the 01 category in the BTAD dataset. All results are generated by PILOT.

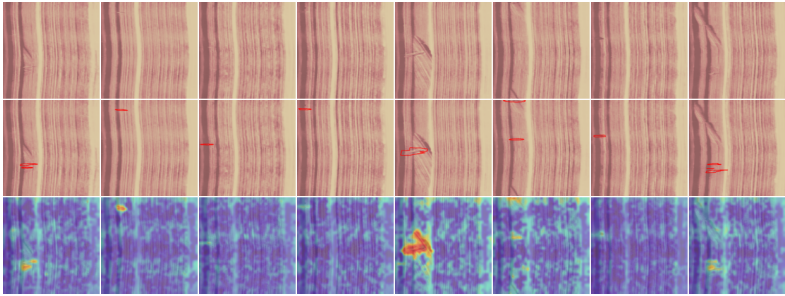


Figure 14: Visualization of input images (top), ground-truth masks (middle), and model-generated anomaly maps (bottom) for the 02 category in the BTAD dataset. All results are generated by PILOT.

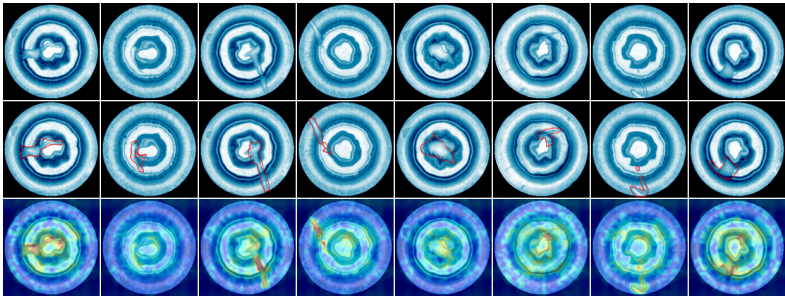


Figure 15: Visualization of input images (top), ground-truth masks (middle), and model-generated anomaly maps (bottom) for the 03 category in the BTAD dataset. All results are generated by PILOT.

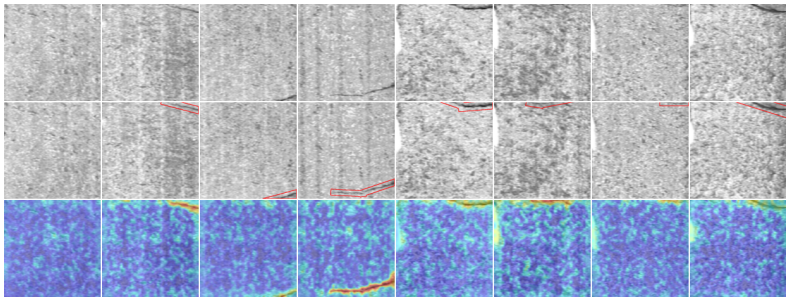


Figure 16: Visualization of input images (top), ground-truth masks (middle), and model-generated anomaly maps (bottom) for the *electrical commutators* category in the SDD dataset. All results are generated by PILOT.

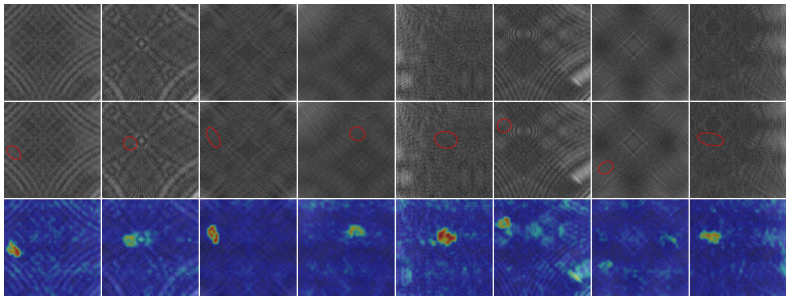


Figure 17: Visualization of input images (top), ground-truth masks (middle), and model-generated anomaly maps (bottom) for the *class 1* category in the DAGM dataset. All results are generated by PILOT.

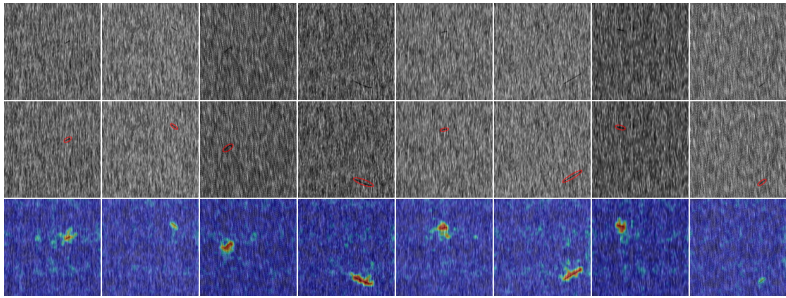


Figure 18: Visualization of input images (top), ground-truth masks (middle), and model-generated anomaly maps (bottom) for the *class 2* category in the DAGM dataset. All results are generated by PILOT.

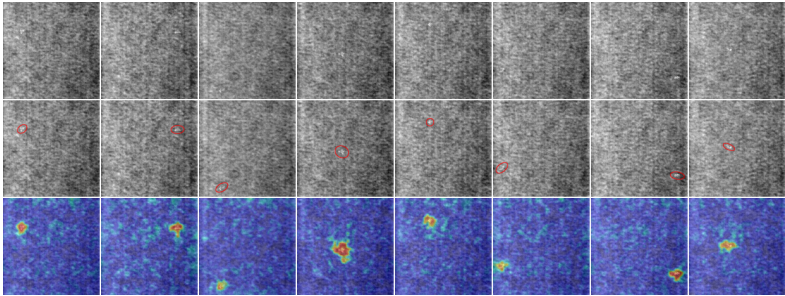


Figure 19: Visualization of input images (top), ground-truth masks (middle), and model-generated anomaly maps (bottom) for the *class 3* category in the DAGM dataset. All results are generated by PILOT.

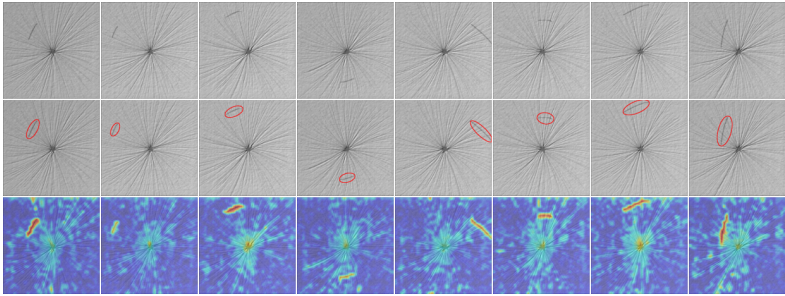


Figure 20: Visualization of input images (top), ground-truth masks (middle), and model-generated anomaly maps (bottom) for the *class 4* category in the DAGM dataset. All results are generated by PILOT.

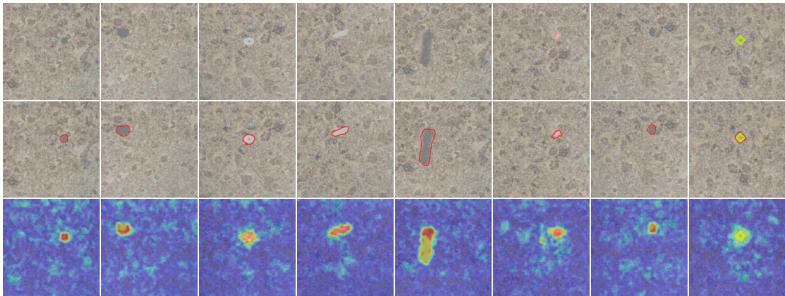


Figure 21: Visualization of input images (top), ground-truth masks (middle), and model-generated anomaly maps (bottom) for the *Blotchy* category in the DTD dataset. All results are generated by PILOT.

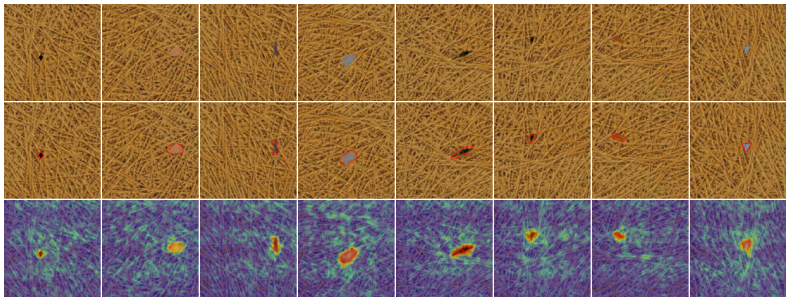


Figure 22: Visualization of input images (top), ground-truth masks (middle), and model-generated anomaly maps (bottom) for the *Fibrous* category in the DTD dataset. All results are generated by PILOT.

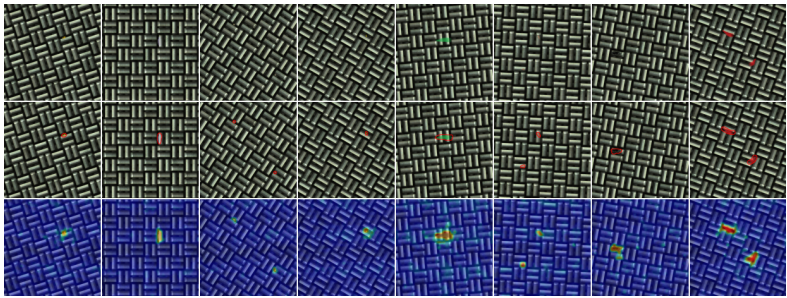


Figure 23: Visualization of input images (top), ground-truth masks (middle), and model-generated anomaly maps (bottom) for the *Woven* category in the DTD dataset. All results are generated by PILOT.

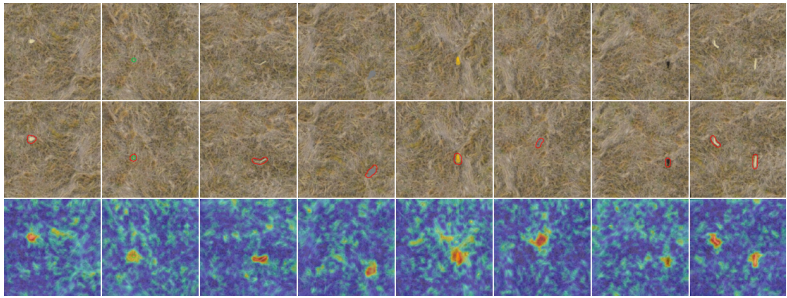


Figure 24: Visualization of input images (top), ground-truth masks (middle), and model-generated anomaly maps (bottom) for the *Matted* category in the DTD dataset. All results are generated by PILOT.

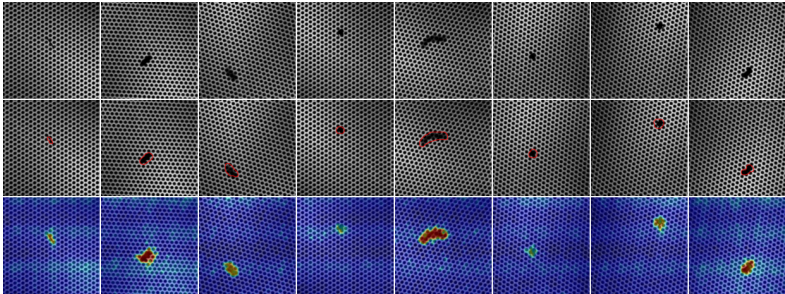


Figure 25: Visualization of input images (top), ground-truth masks (middle), and model-generated anomaly maps (bottom) for the *Perforated* category in the DTD dataset. All results are generated by PILOT.